Supporting Information

Controlling desolvation through polymer-assisted grinding

Maxwell W. Terban, Leillah Madhau, Aurora J. Cruz-Cabeza, Peter O. Okeyo, Martin Etter, Armin Schulz, Jukka Rantanen, Robert E. Dinnebier, Simon J. L. Billinge, Mariarosa Moneghini, and Dritan Hasa

Table of contents:

1. Materials

Anydrous theophylline (**thp**) (99%) and 2-pyrrolidinone (**2-pyr**) (99%) were purchased from Sigma Aldrich. (**thp**)·(**2-pyr**) and 2(**thp**)·3(**2-pyr**) solvates were prepared in house. Poly(acrylic acid) (PAA, Mw= 450,000), Poly(ethylene glycol) (PEG, Mw 1,000), Poly(ethylene glycol) dimethyl ether (PEGDME, Mw=1,000), Kolliphor® P188, Poly(4-vinylpyridine) (P4VP, Mw=60,000), and Polyvinyl alcohol (PVA Mw= 70,000–100,000) were purchased from Sigma Aldrich. Poly(acrylamide) (PAM Mw 5–5,000,000) and polyvinylpyrrolidone K12 (PVP Mw 3,500) were purchased from Fisher Scientific. All materials were used as purchased without further purification.

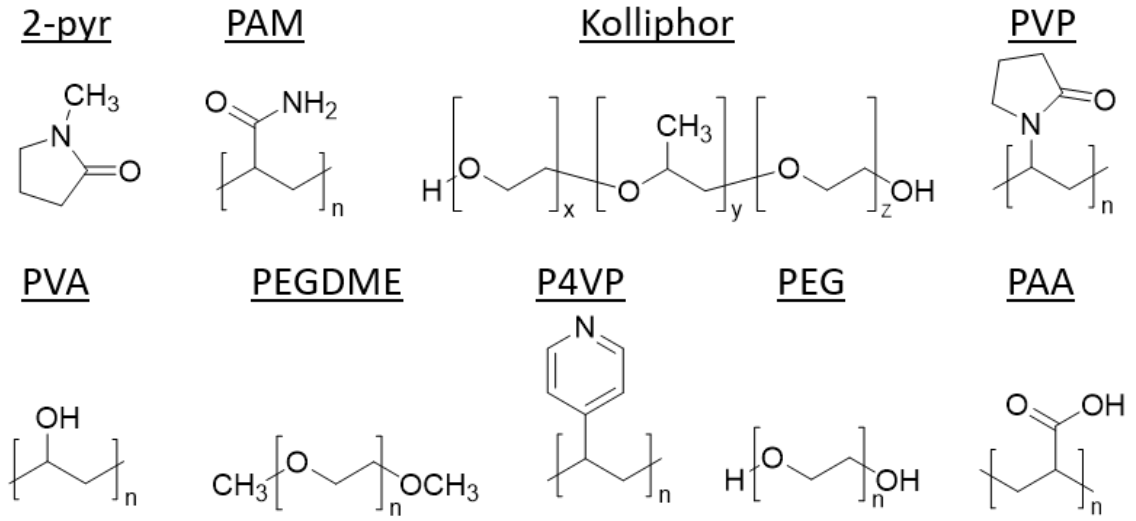

Figure S1. Structures of **2-pyr** and the repeat unit for each polymer tested.

2. Variable-temperature powder diffraction experiments

A PANalytical X'pert PRO x-Ray Diffractometer (purchased from PANalytical B.V., Almelo, Netherlands) consisting of a θ/θ goniometer and a solid state PIXcel detector was used. Nickel-filtered CuKα (λ = 1.5418 Å) generated at a tube voltage of (45 kV) and current (40 mA). A reflection mode between 5° and 35° (scan speed 0.06734° s^{-1} and a step size of 0.0263° 2θ) was employed. The obtained data was analysed using X'Pert Data Collector software (PANalytical, Almelo, Netherlands).

The variable temperature-XRPD measurements were performed with a steel sample holder that has a depth of 0.2 mm. An Anton Paar CHC chamber (Anton Paar GmbH, Graz, Austria) was used. The temperature was controlled using a TCU 110 Anton Paar GmbH controller. A scan speed of 0.328° s^{-1} was used.

3. Mechanochemical experiments

3.1. Polymer screening experiments

3.1.1. POLAG procedure

(**thp**)·(**2-pyr**) or 2(**thp**)·3(**2-pyr**) solvates were prepared mechanochemically using a *Retsch MM200* mixer mill. Specifically, 1.11 x 10^{-3} mole (approximately 200 mg of solid) of anhydrous **thp** were milled for 60 min in the presence of **2-pyr** either in a 1:1 (**in the case of** (**thp**)·(**2-pyr**)) or 2:3 stoichiometry (in the case of 2(**thp**)·3(**2-pyr**)). The purity of each batch was verified using XRPD.

Neat- and polymer-assisted grinding (POLAG) experiments were performed using a *Retsch MM200* mixer mill. In a typical experiment, 200 mg of preformed solvate (either (**thp**)·(**2-pyr**) or 2(**thp**)·3(**2-pyr**)) were added to a 15 mL steel milling jar containing two milling balls (7 mm diameter). Different amounts of liquid additives (δ = 0.05–2) were also added prior to milling. Although **2-pyr** is not a highly volatile liquid,

snap closed grinding jars were used to minimize any liquid evaporation. The mixture was subsequently milled for 60 min at a frequency of 25 Hz.

3.1.2. XRPD measurements

The mechanochemically prepared solids were characterised by x-ray powder diffraction (XRPD) using a *Panalytical X'Pert Pro* diffractometer with Ni-filtered CuK_α radiation at a wavelength of 1.5418 Å equipped with an RTMS X'celerator detector. For each experiment, approximately 20–25 mg of mechanochemical product was gently pressed on a glass slide to give a flat surface. The data were collected in the 3−40° 2θ range using a step size of 0.0334° and a scan speed of 0.142° s^{-1}.

3.1.3. Phase quantification from XRPD patterns

Multiphase Rietveld refinements were performed using TOPAS academic v6[1] over a range of 6–40° 2θ to estimate relative phase fractions resulting from the polymer screening experiments. The background contributions were described using Chebychev polynomials of 6th order and any peaks specifically attributable to the polymer were accounted for using additional single peak contributions added to the background. Lorentz-polarization correction was set to 0 for no monochromator. The instrumental peak shape was described with the TOPAS full axial model. Further peak shape effects were described using Lorentzian and Gaussian strain and crystallite size broadening convolutions. The lattice parameters were refined according to the respective phase symmetries along with a zero error correction to account for sample offset. The data were not suitable for refining the atomic displacement parameter (ADP), which was fixed to 0. Some patterns appeared to have severe preferred orientation effects, so refinements were performed both with and without a spherical harmonics correction of 6th order to estimate the uncertainty of the resulting phase fraction values. The refinement was run by minimizing the residual function R_w, by refining the parameters P of the calculated model, as

$$R_w = \sqrt{\frac{\sum_{i=1}^{n}[I_{obs}(2\theta_i) - I_{calc}(2\theta_i, P)]^2}{\sum_{i=1}^{n} I_{obs}(2\theta_i)^2}}.$$

$R_{w'}$ is the background corrected R_w where the denominator is replaced by $\sum_{i=1}^{n}(I_{obs}(2\theta_i) - Bkg(2\theta_i))^2$.

The trends in the weight percent ($wt.\%$) versus δ were approximated by fitting empirical functions to the sets of datapoints obtained by both fitting procedures. For POLAG mixtures with PAM, Kolliphor, PVP, PVA, PEGDME, P4VP, and PEG, the trends were fit with a decay model defined as

$$wt.\% = a_1 \times [1 - exp\,(-a_2 \times \delta)\,],$$

with fit parameters denoted by a_i. For PAA, the trend of **thp** was fit using an Arrhenius equation defined as

$$wt.\% = a_1 \times exp\left(-\frac{a_2}{\delta}\right),$$

and the trend of **thp**:**2-pyr** monosolvate was fit using a Gamma distribution defined as

$$wt.\% = a_1 \times \delta^{(a_2-1)}\, exp\,(-a_3 \times \delta)\,.$$

3.2. Molecular interaction experiments

3.2.1. POLAG procedure

POLAG samples were prepared by loading the components into a 10 mL stainless tell jar with two 7 mm stainless steel balls. Grinding was performed in a MM400 Retsch shaker mill at 25 Hz for 60 minutes. The sesquisolvate sample was ground separately with each of PAM, PEG, and PAA with $\delta = 0.75$ (~133 mg **thp**:**2-pyr** sesquisolvate to 100 mg polymer). The corresponding amounts of pure **thp** or **2-pyr** were also ground with PAM, PEG, and PAA: 56.7 ml of **2-pyr** or 77 mg of **thp** milled in the presence of 100 mg of the respective polymer. Non-milled PAA, PAM, PEG, **2-pyr**, **thp**, **thp**:**2-pyr** monosolvate, **thp**:**2-pyr** sesquisolvate were also considered as standards for comparison.

3.2.2. XRPD measurements

Laboratory XRPD patterns were collected at room temperature on a STOE Stadi-P diffractometer with Cu$K_{\alpha 1}$ radiation ($\lambda = 1.540596$ Å), a Ge(111) Johann monochromator, and an array of three DECTRIS Mythen 1K detectors for continuous coverage over a range of roughly 0.0–55.06° 2θ. The samples were held as a film of powder and measured in a transmission geometry with the sample rotated on an axis parallel to the incident beam. Data were collected for a total counting time of 600 s.

3.2.3. Rietveld refinements

Rietveld refinements were performed using TOPAS academic v6.[1] The background contributions were described using Chebychev polynomials of 11th order. Lorentz-polarization correction was set to 27.3 according to the Ge(111) Johann monochromator. The instrumental peak shape was described with the TOPAS full axial model, with the parameters refined for **thp** sesquisolvate and then fixed for all other samples. Further peak shape effects were described using Lorentzian and Gaussian strain and crystallite size broadening convolutions. The lattice parameters were refined according to the respective structure model symmetry along with a zero error correction to account for detector/sample offset. A single isotropic atomic displacement parameter (ADP) was considered each phase. A global scale factor was refined, and a 2nd order spherical harmonics correction was used to correct slight deviations in relative peak intensities, which could occur due to some preferred orientation effects from the transmission geometry used. Relative values of the crystallite sizes were estimated by a fit to the first three Bragg peaks, without strain parameters, and the values estimated by the integral breadth based column heights are **thp** (170±40 nm), **thp**-PEG (80±10 nm), 2(**thp**)·3(**2-pyr**)-PAA (70±20 nm), **thp**-PAM (30±10 nm), **thp**-PAA (20±10 nm). Errors given as estimated standard deviations from the refinements multiplied by a factor of 10.

3.2.4. X-ray total scattering measurements

Total scattering measurements were carried out using P02.1, the Powder Diffraction and Total Scattering Beamline, at PETRA III of the Deutsches Elektronen-Synchrotron (DESY). The rapid acquisition PDF method (RAPDF)[2] was used with a large-area 2D PerkinElmer detector (2048×2048 pixels, 200×200 μm each) and sample-to-detector distance of 303.3964 mm. The incident energy of the x-rays was 59.858 keV ($\lambda = 0.20713$ Å). Samples were loaded into 1.8 mm inner diameter polyimide capillaries. An empty capillary was measured as background and subtracted, and a Si standard was measured at room temperature for calibration of the setup.

3.2.5. Pair distribution function data processing

Calibration, polarization correction, and azimuthal integration of the 2D scattering data were performed using the software Fit2D.[3] Further correction and normalization of the resulting 1D scattering intensities were carried

out to obtain the total scattering structure function, $F(Q)$, which was Fourier transformed to obtain the PDF, $G(r)$ using PDFgetX3 within xPDFsuite.[4, 5] The maximum value used in the Fourier transform of the total scattering data was 22.5 Å^{-1}. In general, the total scattering structure function $S(Q)$ is obtained from the coherent scattering intensities $I_c(Q)$, after normalization by

$$S(Q) = \frac{I_c(Q)/N - \langle f_i(Q)^2 \rangle + \langle f_i(Q) \rangle^2}{\langle f_i(Q) \rangle^2},$$

where N is the number of scatterers, and Q is the magnitude of the elastic scattering momentum transfer ($Q = 4\pi \sin(\theta)/\lambda$, where λ is the wavelength and 2θ is the scattering angle). $f_i(Q)$ is the atomic form factor for atom i, and averaging denoted by $\langle ... \rangle$ is performed stoichiometrically over all atom species in the sample. The experimental PDF, denoted $G(r)$, is the truncated Fourier transform of the reduced, total scattering structure function, $F(Q) = Q[S(Q) - 1]$, as

$$G(r) = \frac{2}{\pi} \int_{Q_{min}}^{Q_{max}} F(Q) sin(Qr) dQ,$$

where $G(r)$ is the magnitude of the scattering momentum transfer. In practice, values of Q_{min} and Q_{max} are determined by the experimental setup, and Q_{max} is often reduced below the experimental maximum to reduce the effects of low signal-to-noise in the high-Q region on the Fourier transformation.

3.2.6. Real-space structure refinement to the PDFs

The PDF gives the scaled probability of finding two atoms in a material a distance r apart and is relative to the density of atom pairs in the material. Crystal structure model refinements to the real-space PDFs were performed using TOPAS academic v6[6] over a range of 1.2–50 Å. A Gaussian damping term was used to model the effects of instrumental resolution on the real space signal, and convolution with a sinc function was used to account for the peak broadening and termination ripples associated with the Q_{max} value of the range used in the Fourier transformation of the data. The lattice parameters associated with the respective structure models were refined along with a scale factor. The **thp** and **2-pyr** molecules in the structures were set up as rigid bodies from the published crystal structure models using a point_for_site notation in Cartesian coordinates and allowing a single isotropic molecular expansion/contraction factor, which remained ~1.00 in all refinements, and separate rotation (×3) and translation (×3) parameters. Separate intermolecular and intramolecular ADPs were used for **thp** and **2-pyr** molecules respectively. For the intramolecular ADPs, all non-H atom-pairs within the molecule were assigned the intramolecular ADP, while pairs with H atoms were assigned the intramolecular ADP only with the N or C atom it is directly connected to and the intermolecular ADP otherwise.

3.2.7. Raman spectroscopy

Raman spectra of all samples were recorded using a Jobin Yvon Typ V 010 LabRAM single grating spectrometer, equipped with a double super razor edge filter and a Peltier-cooled charge-coupled device camera. The resolution of the spectrometer (grating, 1800 lines/mm) was 1cm^{-1}. The spectra were taken in a quasi-backscattering geometry using the linearly polarized 632.817-nm line of a He/Ne gas laser, over a range of ~50–4000 cm^{-1}. The maximal used power was 4 mW, to protect against local heating. The spot size was 5–10 µm, focused by a 100x microscope objective on to the surface of the sample.

3.2.8. Raman/XRPD/PDF pattern fitting

Pattern fitting was used to index the features and extent of agreement between POLAG mixtures and weighted sums of the pure component or binary mixture patterns. In all cases, the refinements were performed using home-written Python codes using, in particular, the minimization routines from scipy.optimize.curve_fit.

4. Results

4.1. VT-XRPD section

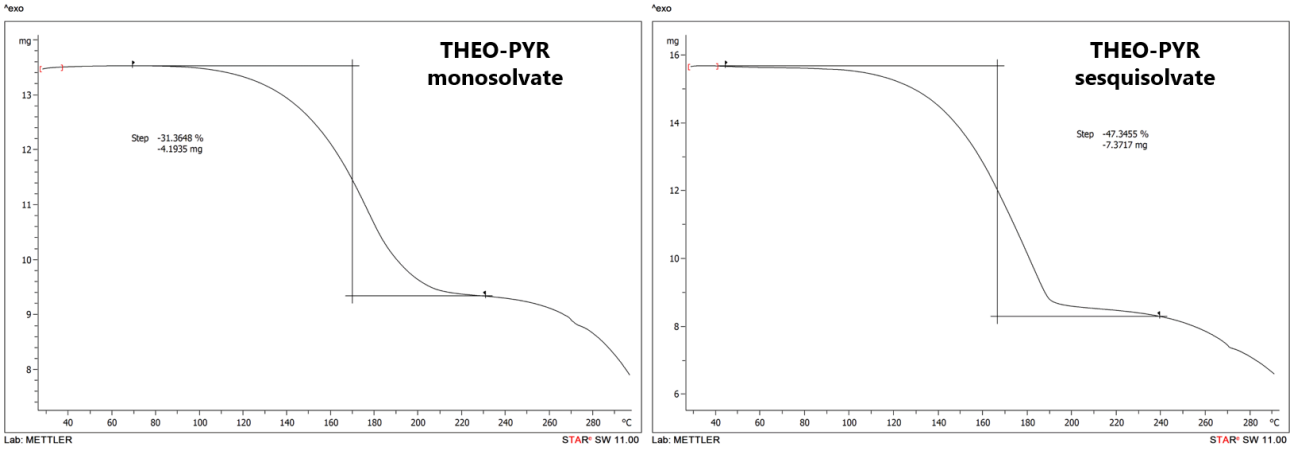

Figure S2. Results of thermogravimetric analysis of **thp**:**2-pyr** monosolvate and sesquisolvate as reported in supporting information of Hasa et al.[7]

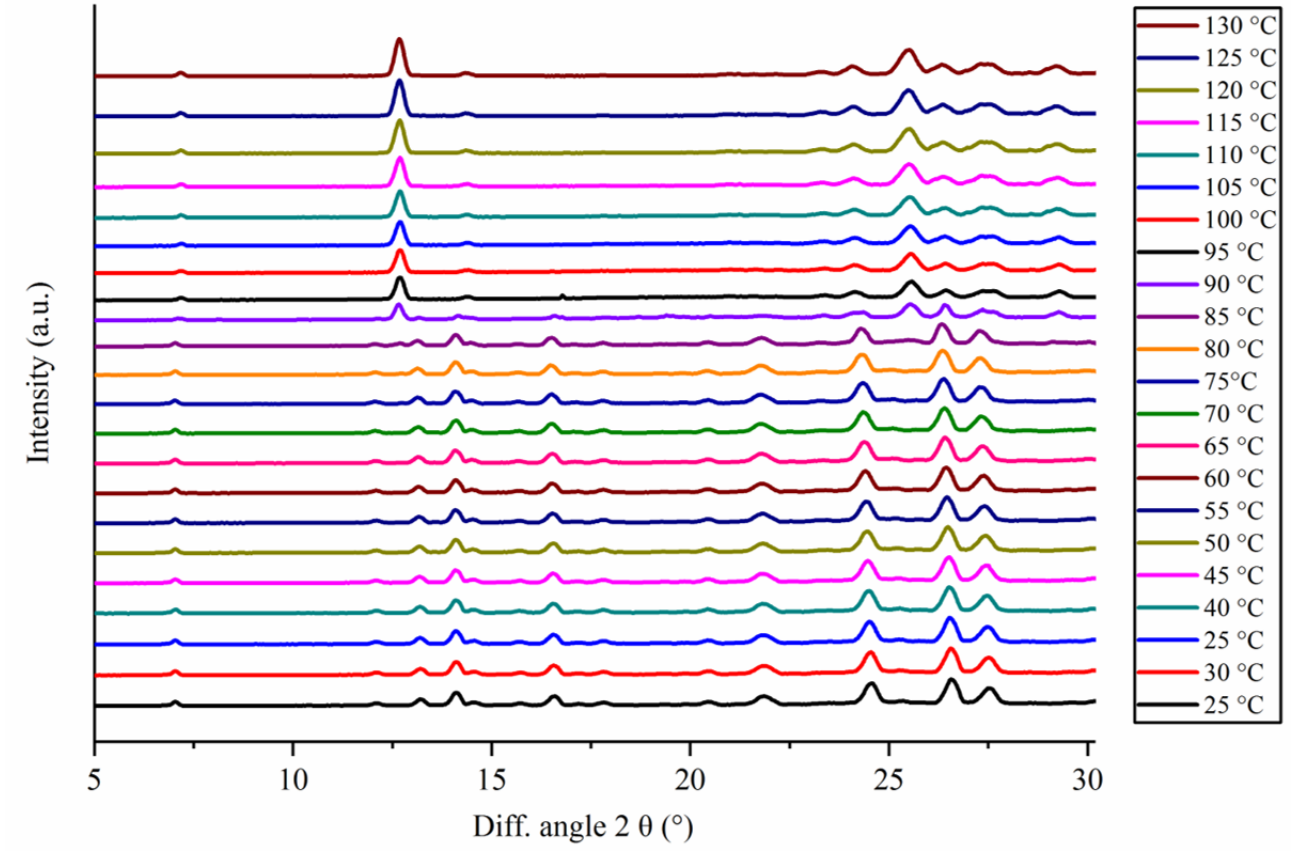

Figure S3. Variable-temperature x-ray powder diffraction (VT-XRPD) experiments using a heating rate of 5 ºC/min.

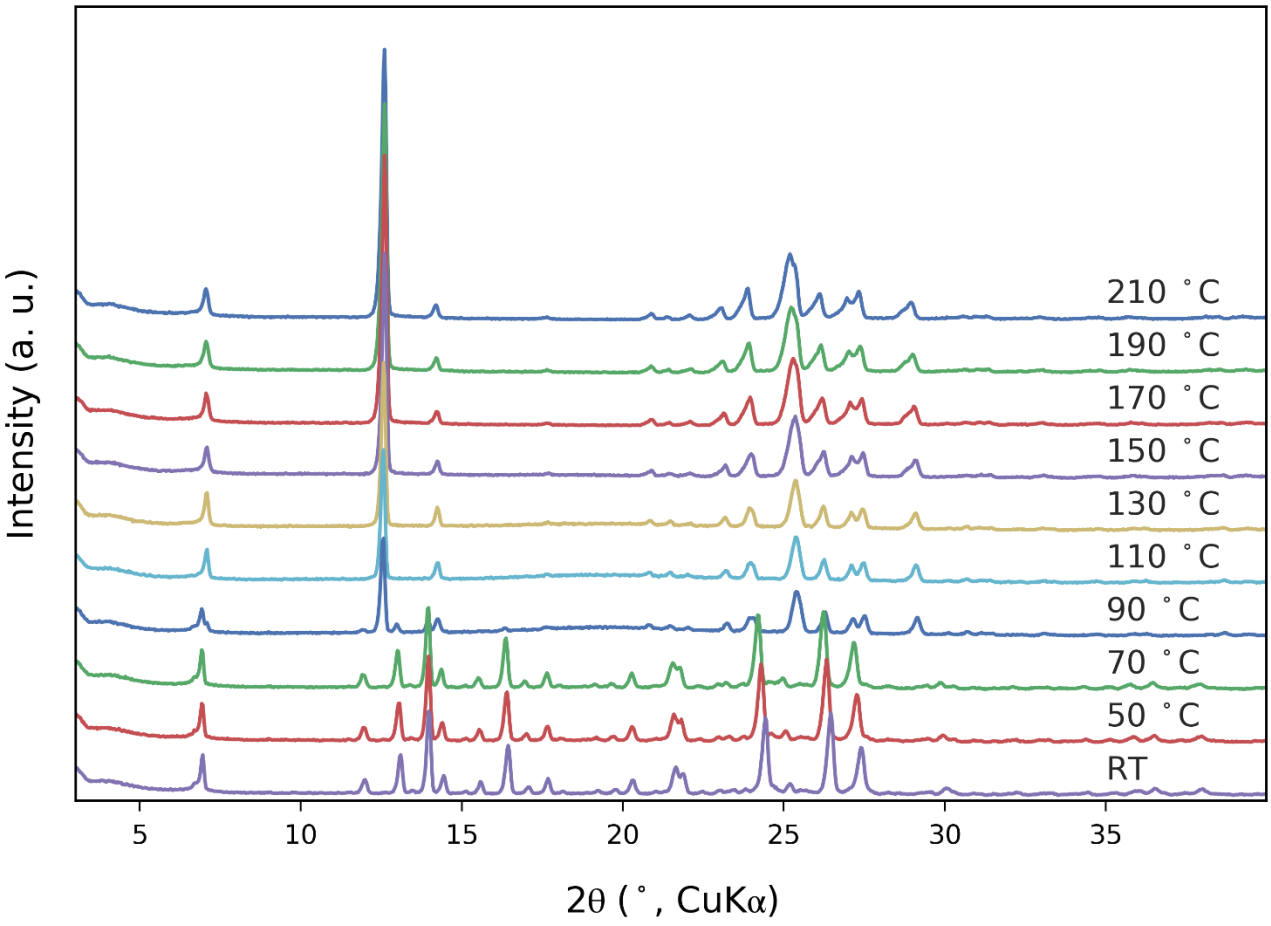

Figure S4. Variable-temperature x-ray powder diffraction (VT-XRPD) experiments using a heating rate of 10 ºC/min (measurements recorded every 20 ºC).

4.2. XRPD patterns associated with polymer screening study

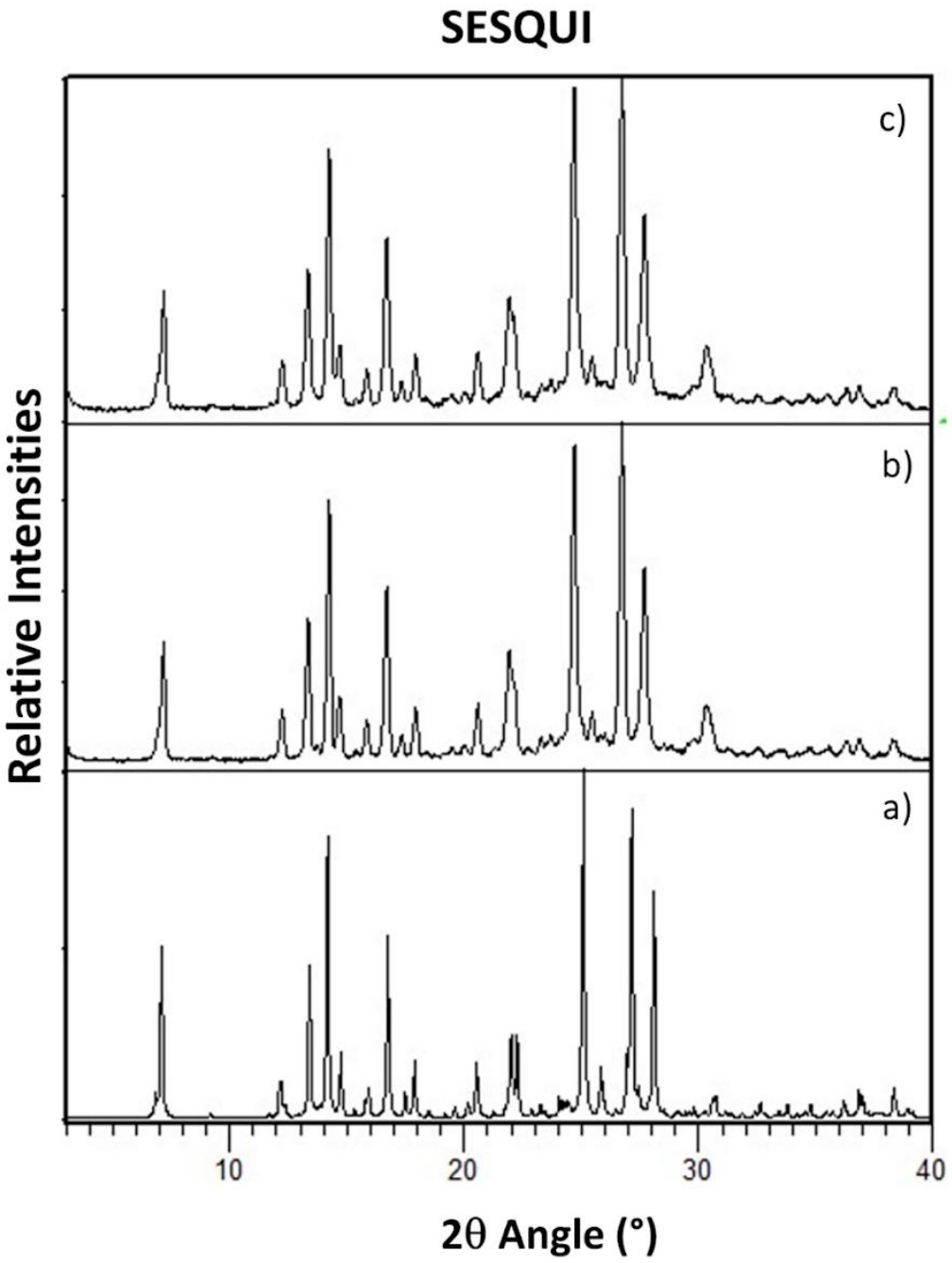

Figure S5. XRPD patterns of (a) calculated and (b) experimental 2(**thp**)·3(**2-pyr**), and (c) solid product obtained after neatly milling preformed 2(**thp**)·3(**2-pyr**) for 60 min at 25 Hz.

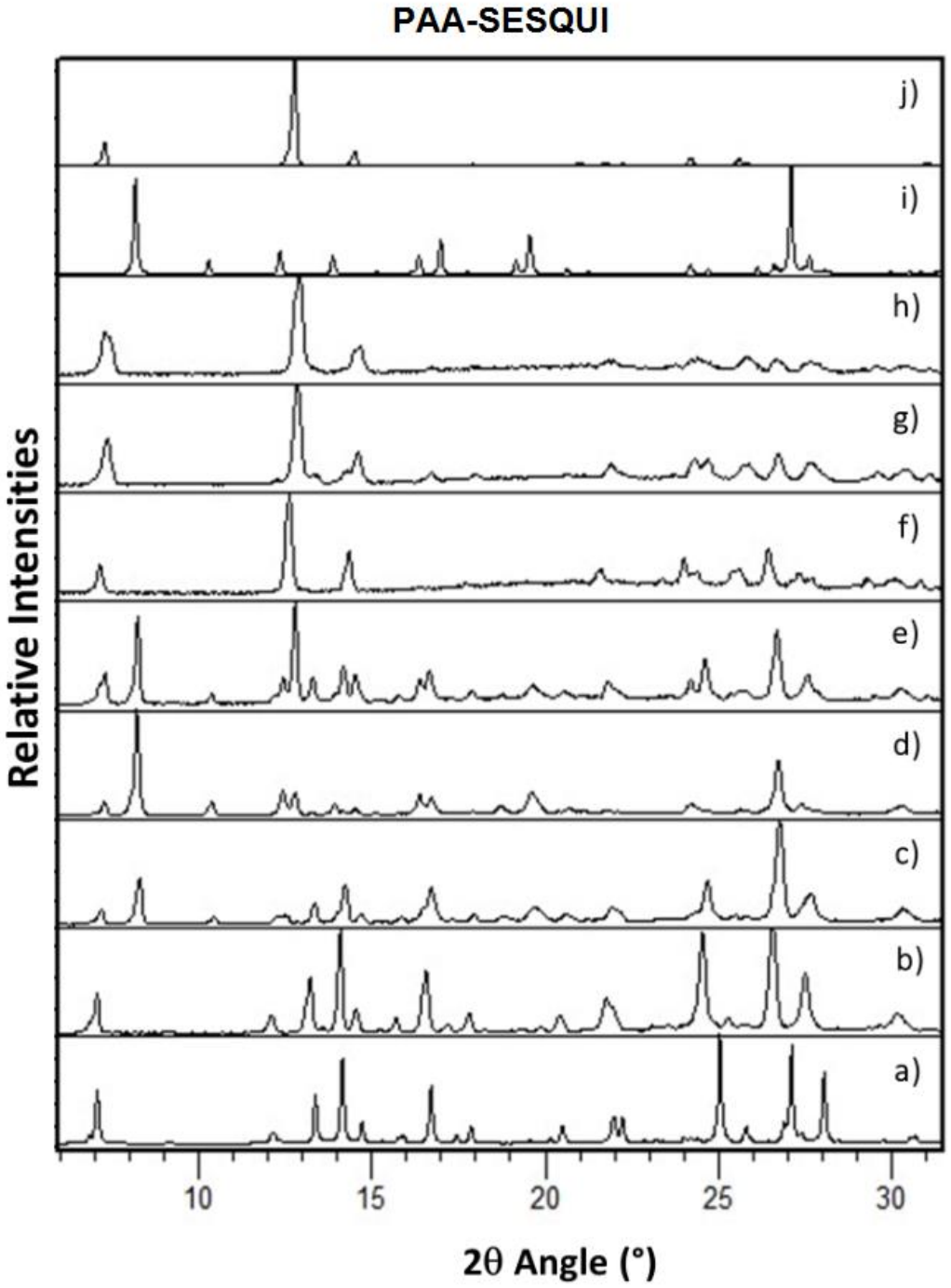

Figure S6. XRPD patterns of (a) calculated and (b) experimental 2(**thp**)·3(**2-pyr**), (c), (d), (e), (f), (g) and (h) products obtained through POLAG of 2(**thp**)·3(**2-pyr**) in the presence of PAA at *d* values of 0.05, 0.10, 0.25, 0.35, 0.50 and 0.75, respectively, (i) calculated (**thp**)·(**2-pyr**) and (j) pure **thp**.

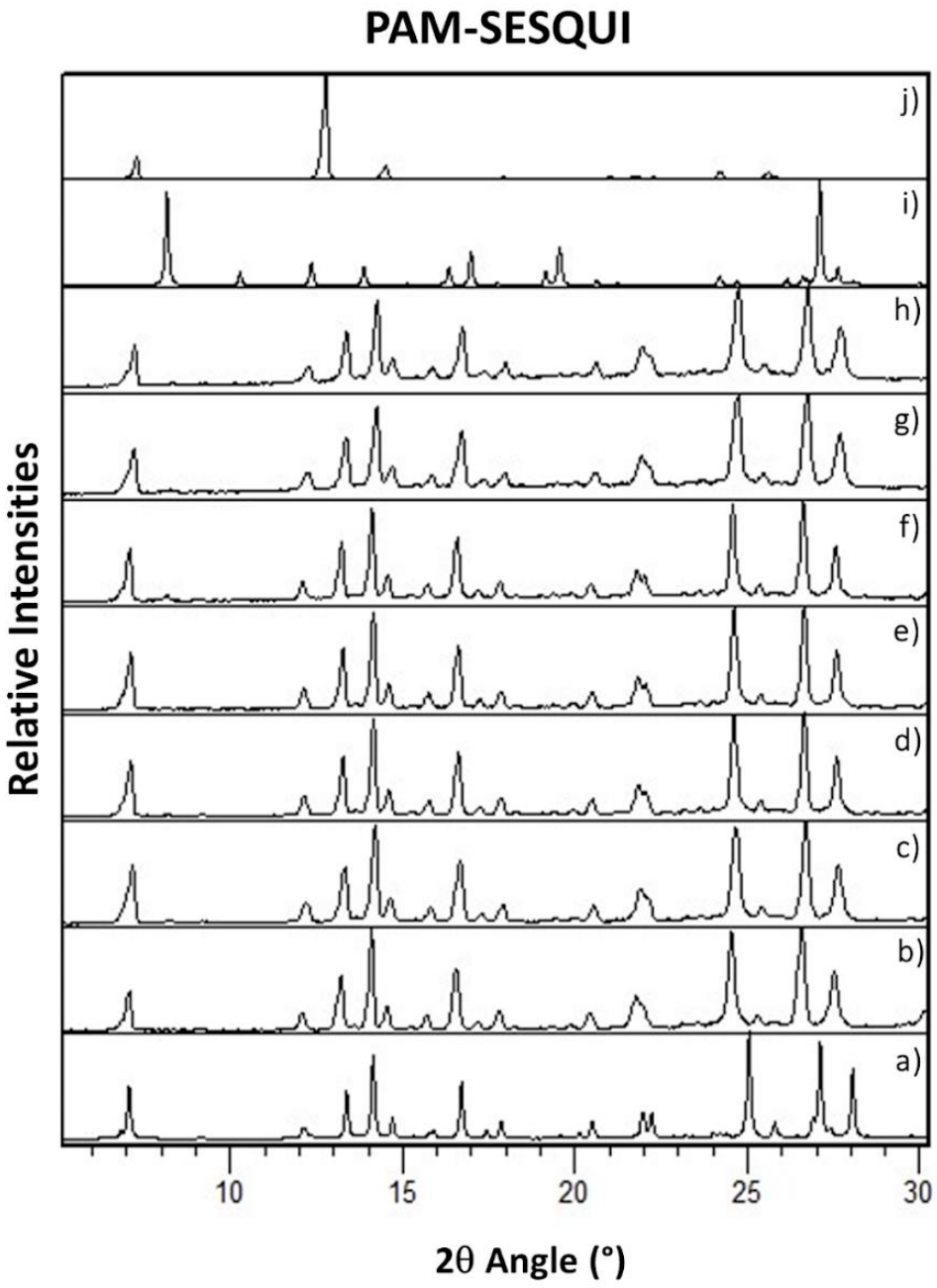

Figure S7. XRPD patterns of (a) calculated and (b) experimental 2(**thp**)·3(**2-pyr**), (c), (d), (e), (f), (g) and (h) products obtained through POLAG of 2(**thp**)·3(**2-pyr**) in the presence of PAM at *d* values of 0.05, 0.10, 0.25, 0.35, 0.50 and 0.75, respectively, (i) calculated (**thp**)·(**2-pyr**) and (j) pure **thp**.

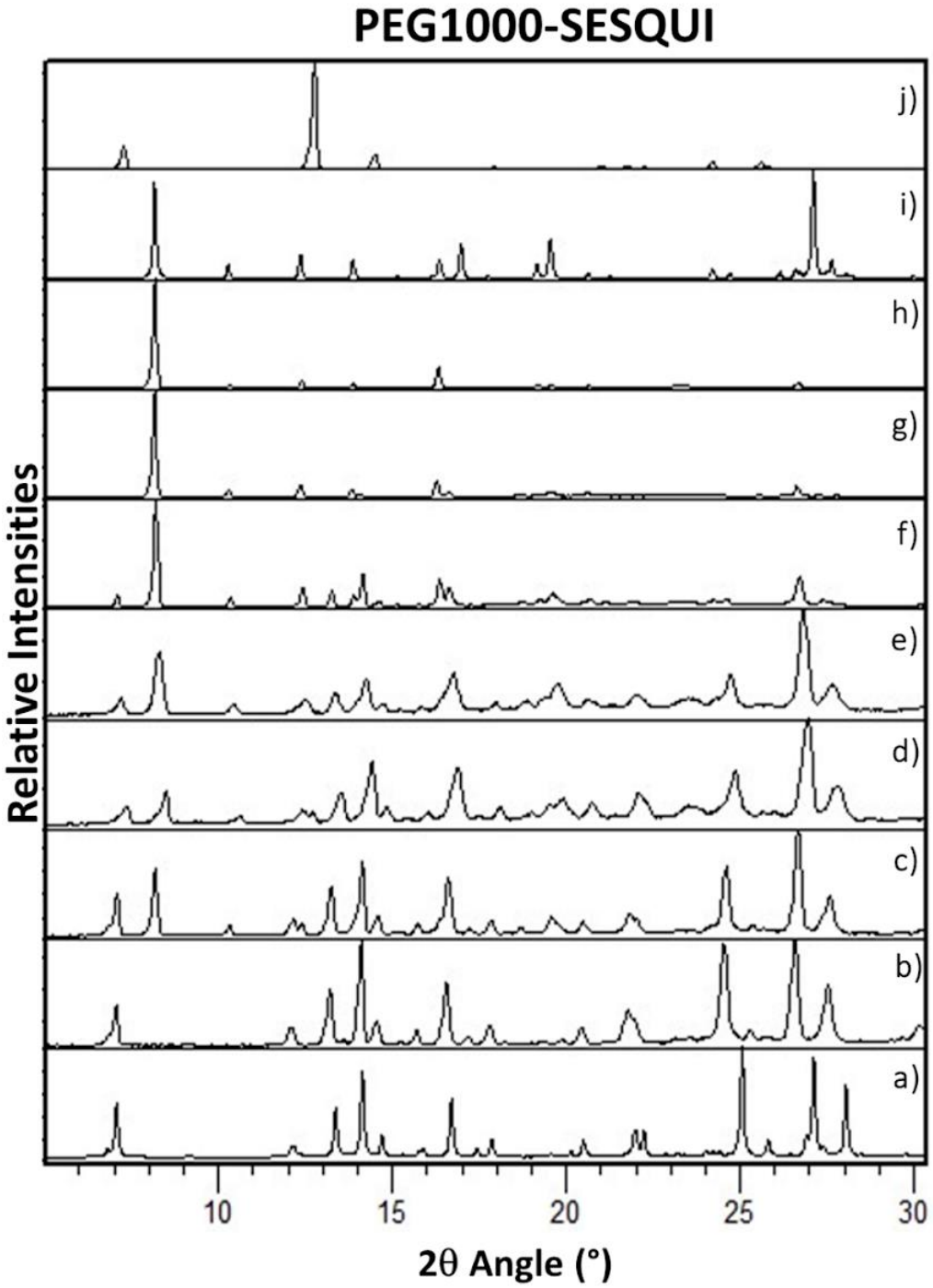

Figure S8. XRPD patterns of (a) calculated and (b) experimental 2(**thp**)·3(**2-pyr**), (c), (d), (e), (f), (g) and (h) products obtained through POLAG of 2(**thp**)·3(**2-pyr**) in the presence of PEG 1,000 at δ values of 0.05, 0.10, 0.25, 0.35, 0.50 and 0.75, respectively, (i) calculated (**thp**)·(**2-pyr**) and (j) pure **thp**.

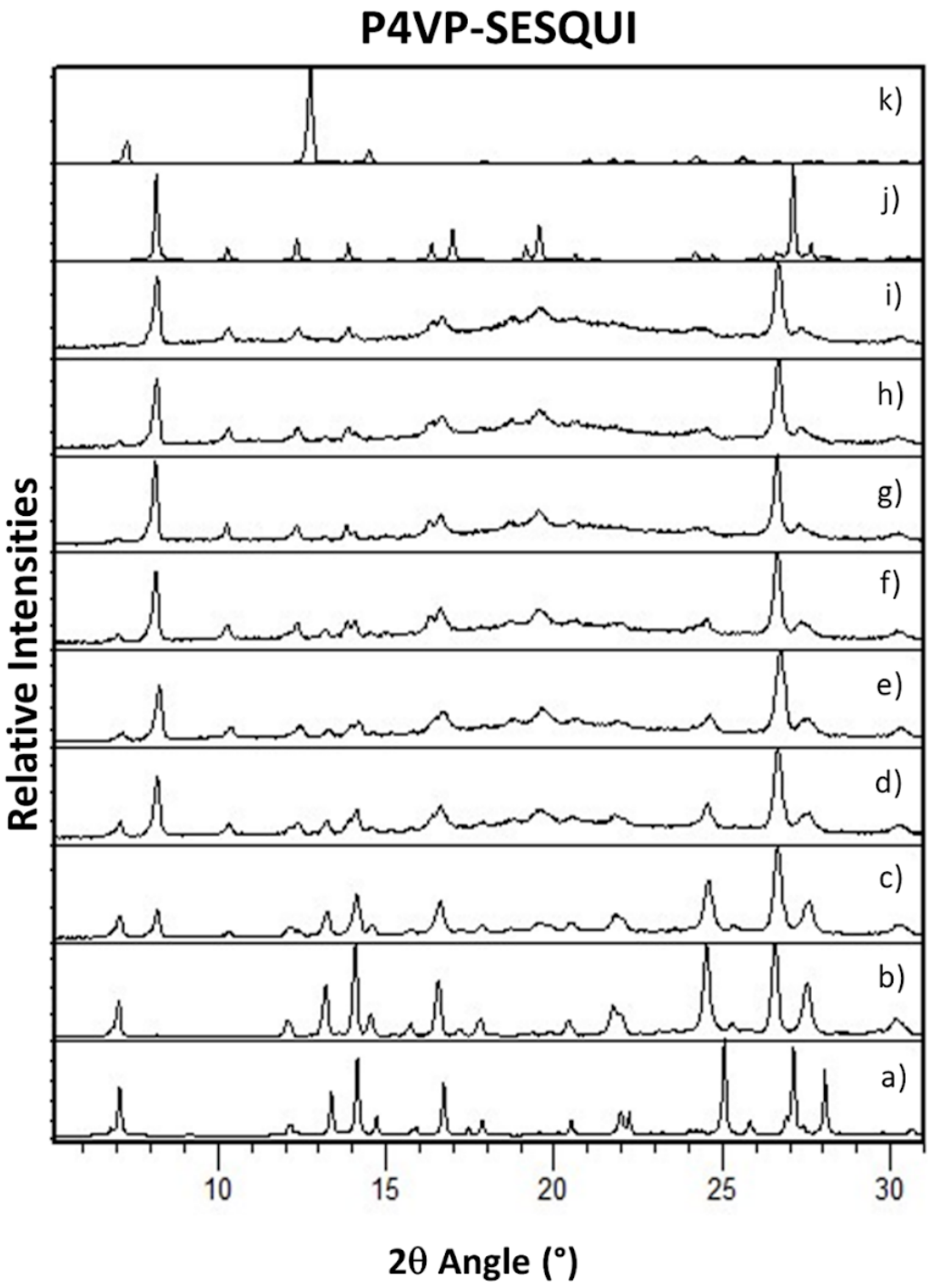

Figure S9. XRPD patterns of (a) calculated and (b) experimental 2(**thp**)·3(**2-pyr**), (c), (d), (e), (f), (g), (h) and (i) products obtained through POLAG of 2(**thp**)·3(**2-pyr**) in the presence of P4VP at δ values of 0.05, 0.10, 0.25, 0.35, 0.50, 0.75 and 2.00, respectively, (j) calculated (**thp**)·(**2-pyr**) and (k) pure **thp**.

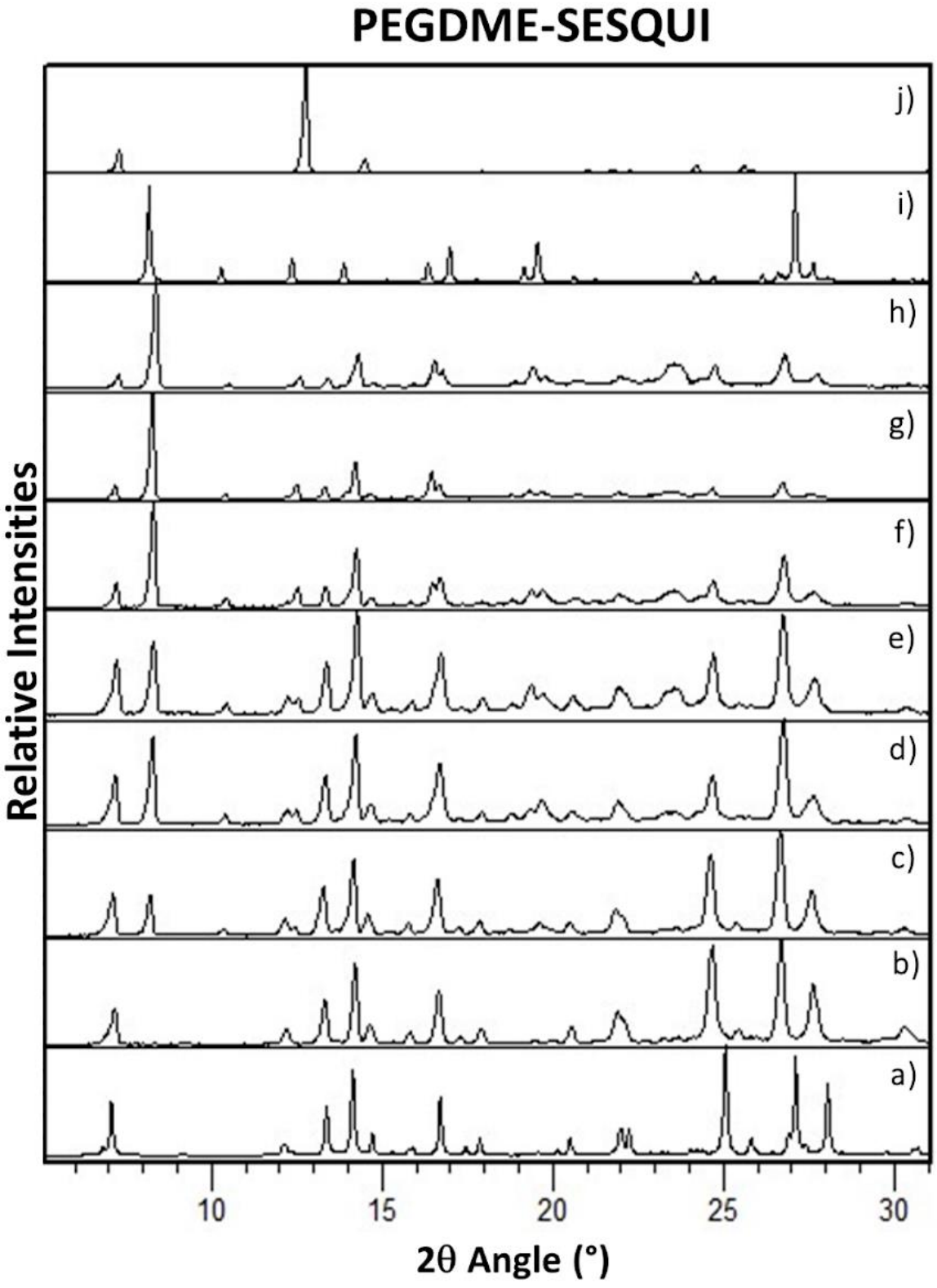

Figure S10. XRPD patterns of (a) calculated and (b) experimental 2(**thp**)·3(**2-pyr**), (c), (d), (e), (f), (g) and (h) products obtained through POLAG of 2(**thp**)·3(**2-pyr**) in the presence of PEGDME at δ values of 0.05, 0.10, 0.25, 0.35, 0.50 and 0.75, respectively, (i) calculated (**thp**)·(**2-pyr**) and (j) pure **thp**.

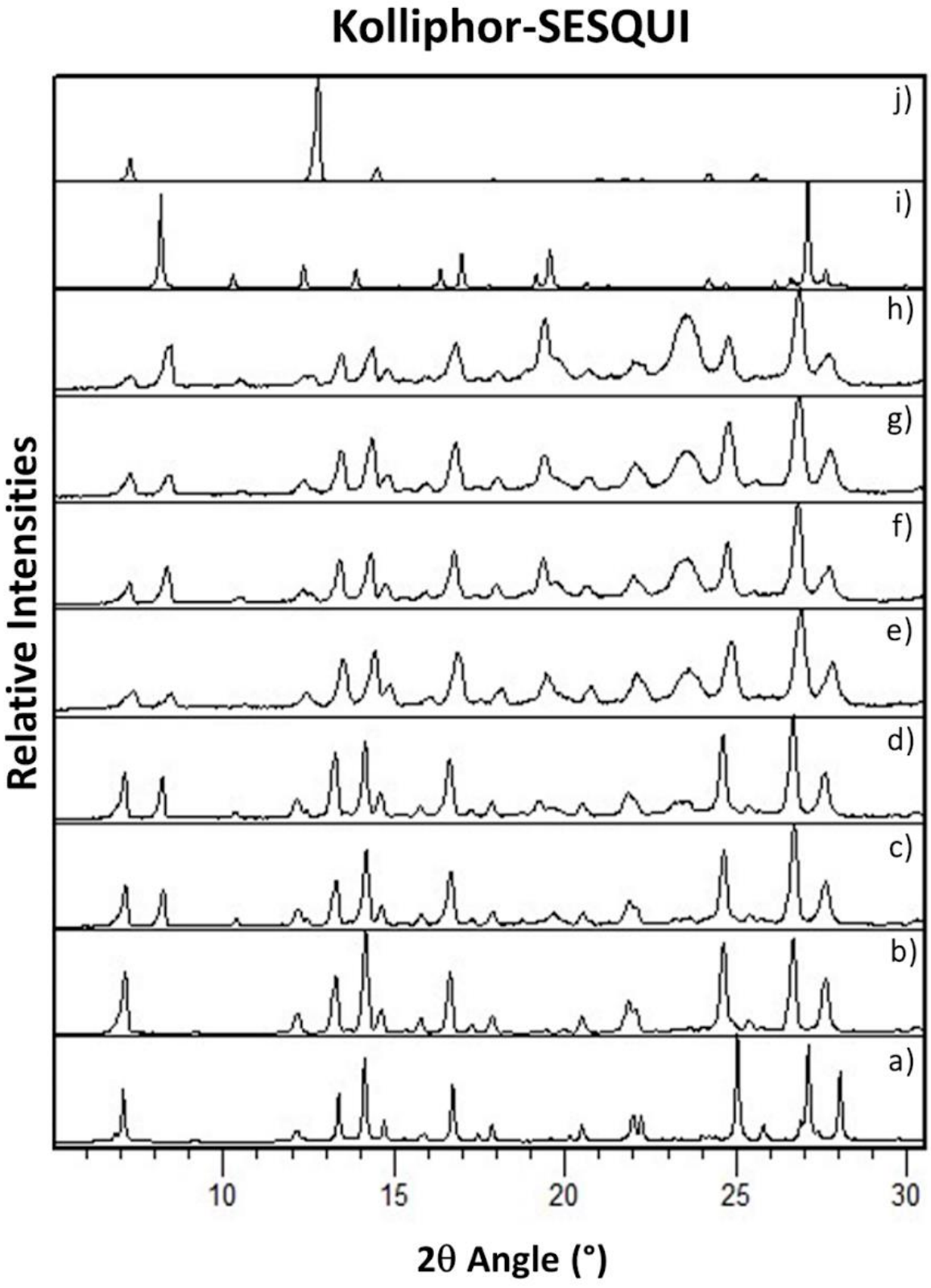

Figure S11. XRPD patterns of (a) calculated and (b) experimental 2(**thp**)·3(**2-pyr**), (c), (d), (e), (f), (g) and (h) products obtained through POLAG of 2(**thp**)·3(**2-pyr**) in the presence of Kolliphor® P188 at δ values of 0.05, 0.10, 0.25, 0.35, 0.50 and 0.75, respectively, (i) calculated (**thp**)·(**2-pyr**) and (j) pure **thp**.

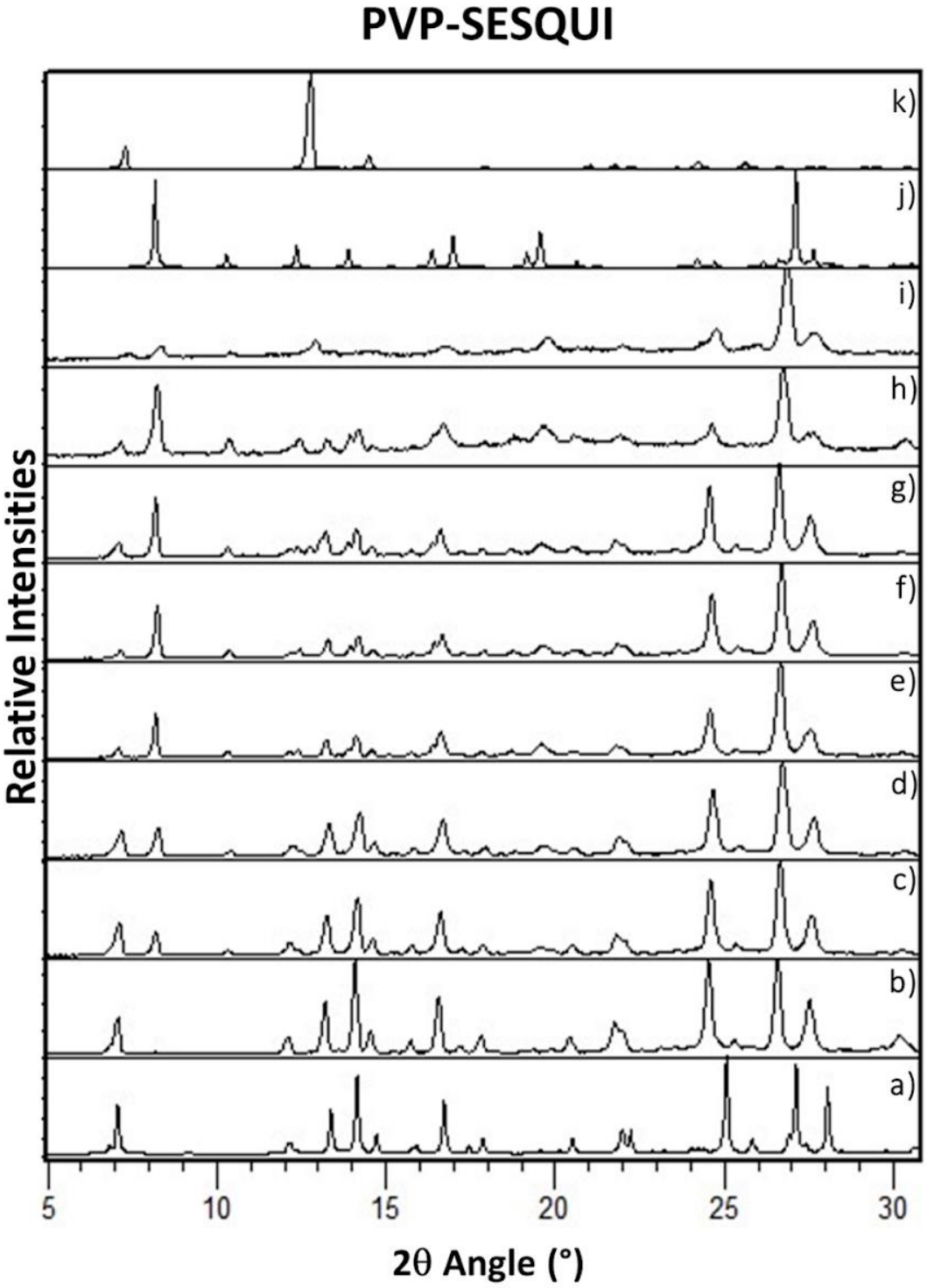

Figure S12. XRPD patterns of (a) calculated and (b) experimental 2(**thp**)·3(**2-pyr**), (c), (d), (e), (f), (g), (h) and (i) products obtained through POLAG of 2(**thp**)·3(**2-pyr**) in the presence of PVP at δ values of 0.05, 0.10, 0.25, 0.35, 0.50, 0.75 and 2.00, respectively, (j) calculated (**thp**)·(**2-pyr**) and (k) pure **thp**.

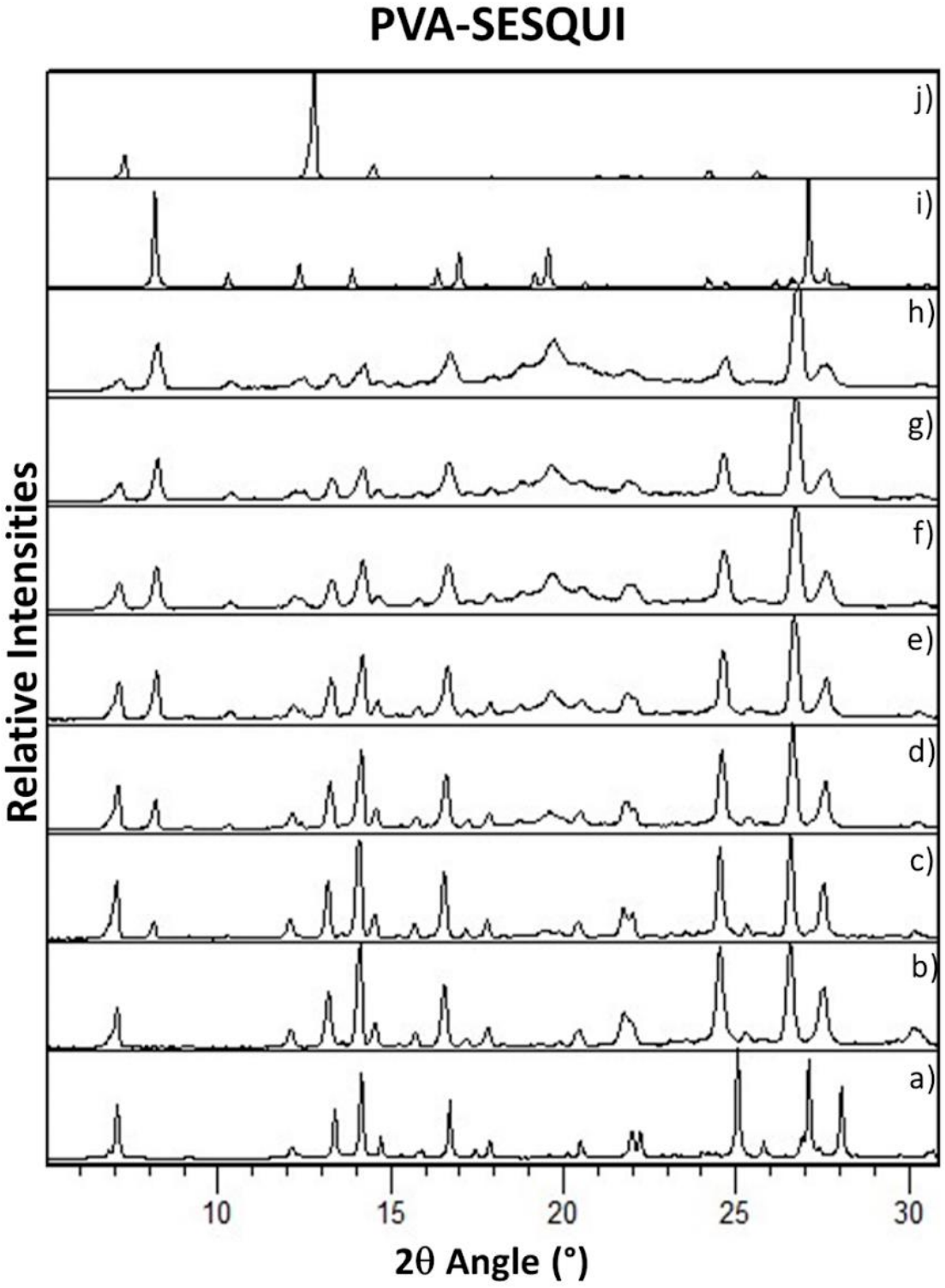

Figure S13. XRPD patterns of (a) calculated and (b) experimental 2(**thp**)·3(**2-pyr**), (c), (d), (e), (f), (g) and (h) products obtained through POLAG of 2(**thp**)·3(**2-pyr**) in the presence of PVA at δ values of 0.05, 0.10, 0.25, 0.35, 0.50 and 0.75, respectively, (i) calculated (**thp**)·(**2-pyr**) and (j) pure **thp**.

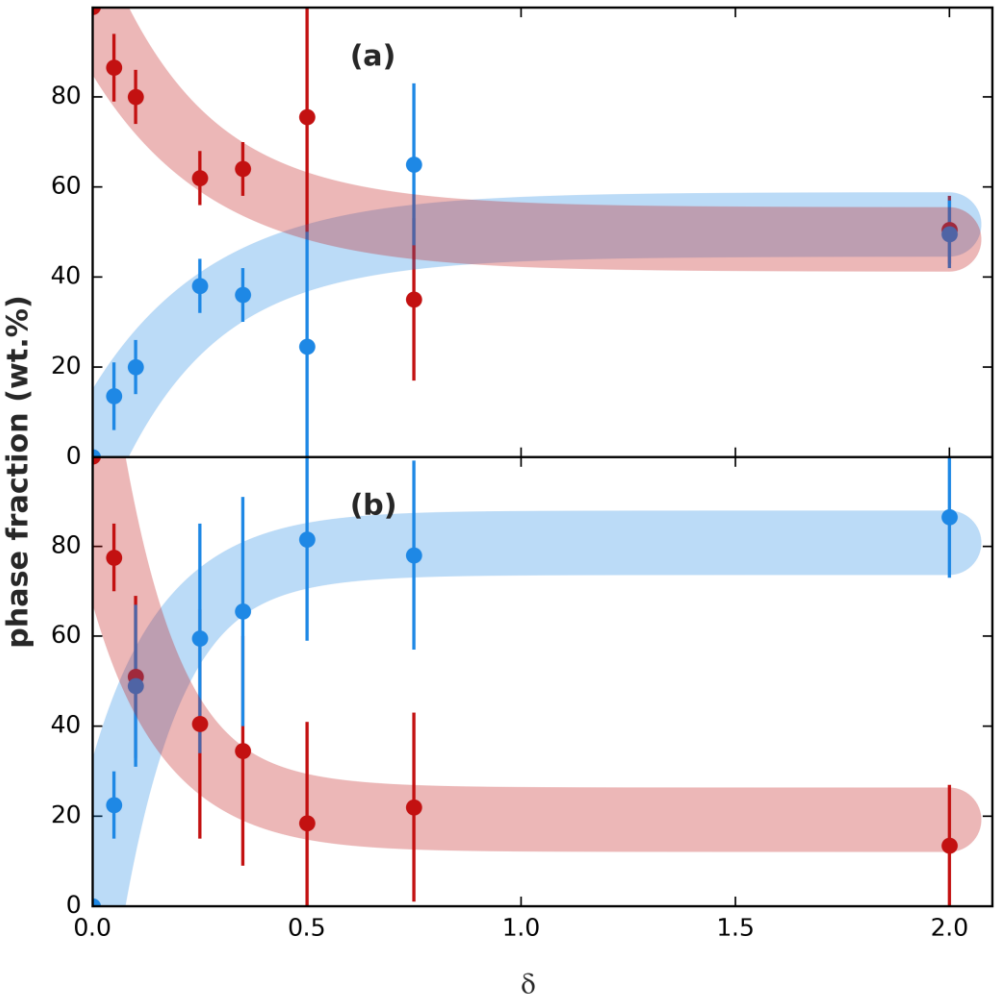

Figure S14. Relative phase fractions of 2(**thp**)·3(2-pyr) and (**thp**)·(**2-pyr**) with qualitative trends (thick shaded lines) of solid products processed for 60 min in the presence of different amounts (given as a function of δ – extended to a value of 2.0) of (a) PVP and (b) P4VP. Bars on the data points represent three standard deviations of the extracted values, and the trends were roughly approximated by fitting an appropriately shaped function to the extracted phase fractions (see SI Section 3.1.3).

4.3. Rietveld refinements to XRPD patterns for molecular interaction study

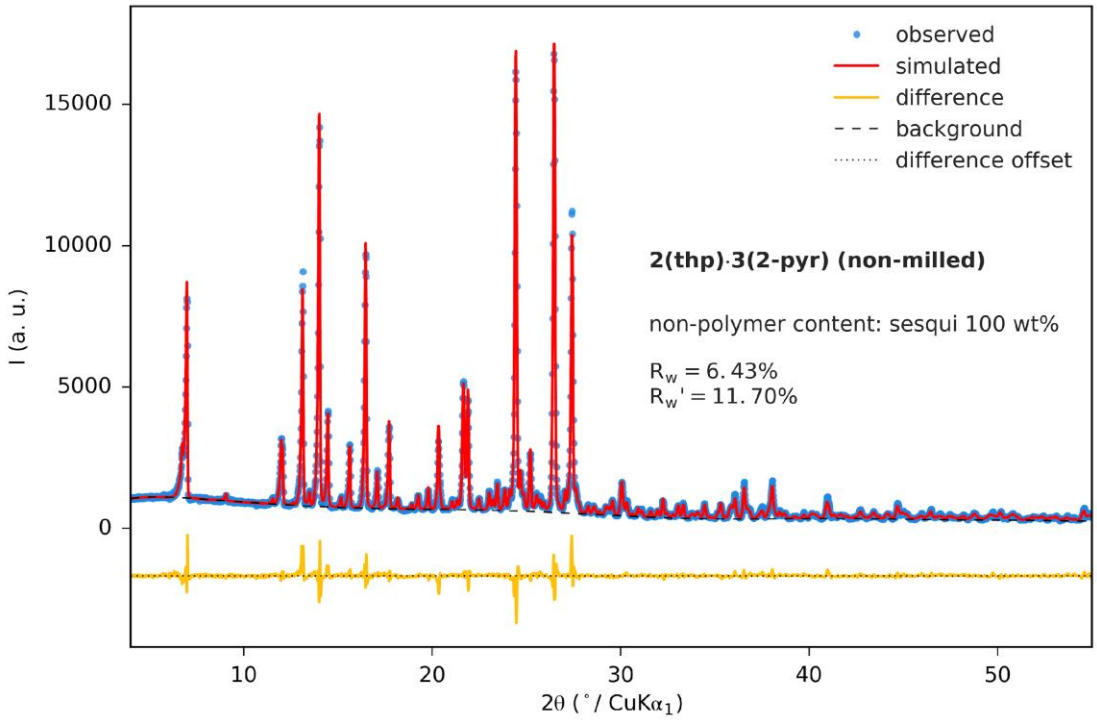

Figure S15: Rietveld refinement of the crystal structure of **thp**:**2-pyr** sesquisolvate (**sesqui**) to the non-milled sample of **sesqui**.

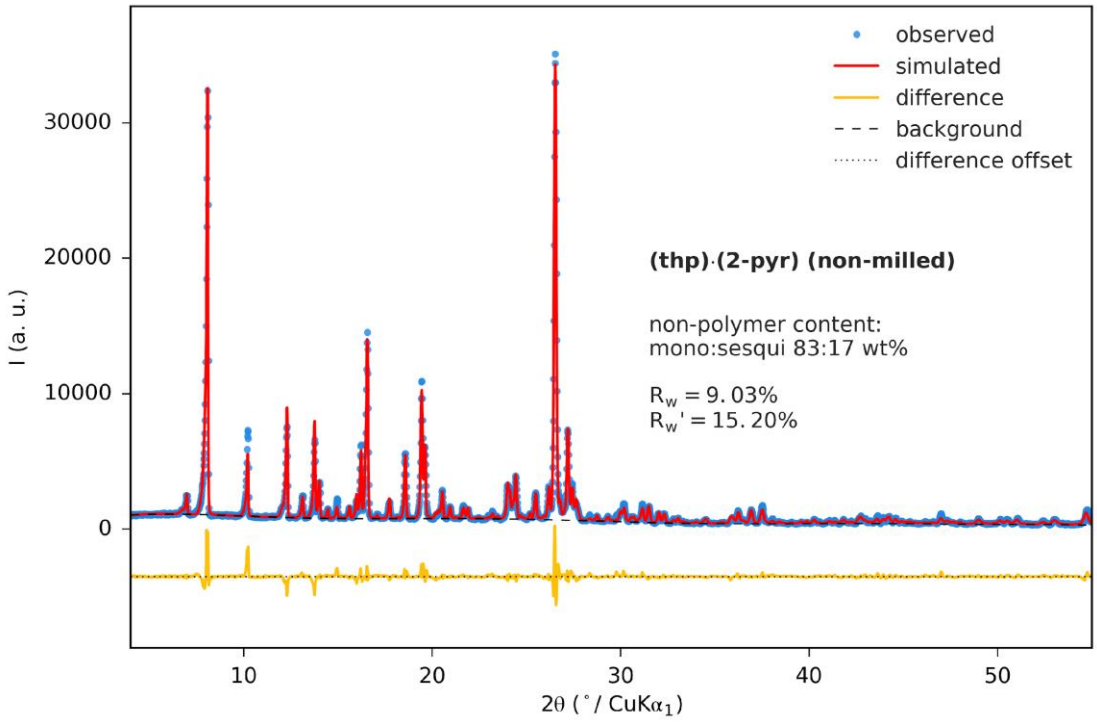

Figure S16: Multiphase Rietveld refinement of the crystal structures of **thp**:**2-pyr** monosolvate (**mono**) and **thp**:**2-pyr** sesquisolvate (**sesqui**) to the non-milled sample of **mono**.

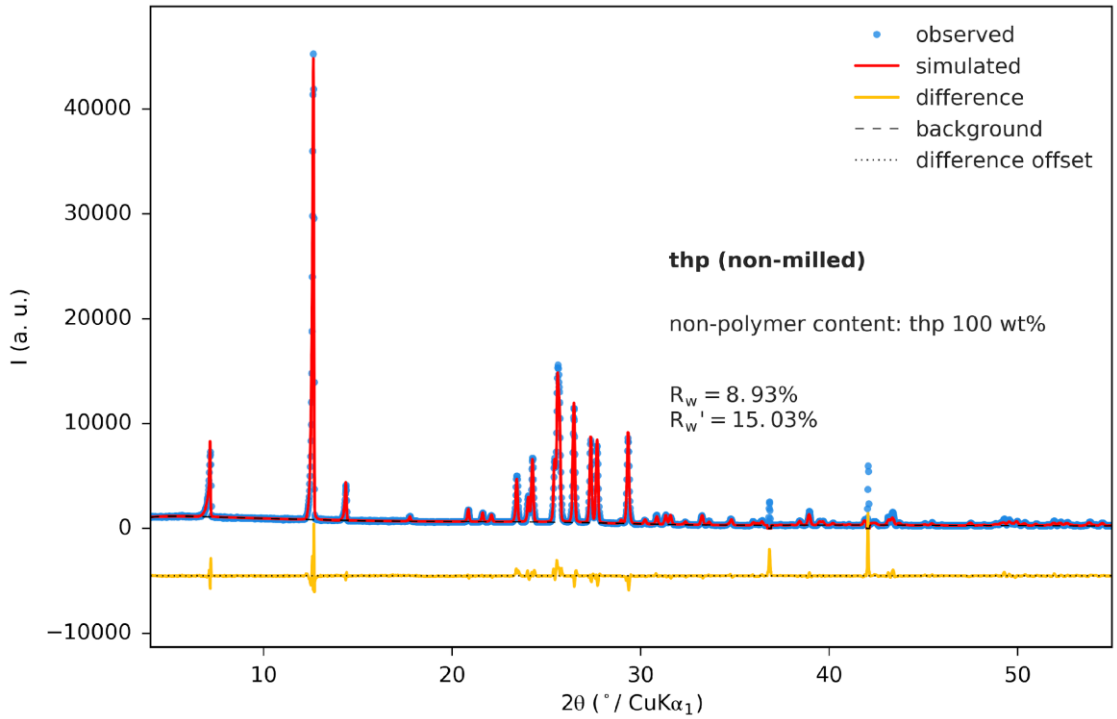

Figure S17: Rietveld refinement of the crystal structure of **thp** to the non-milled sample of **thp**. The spikes at approximately 37 and 42° are aberrations from the detector, which were excluded from the refinement.

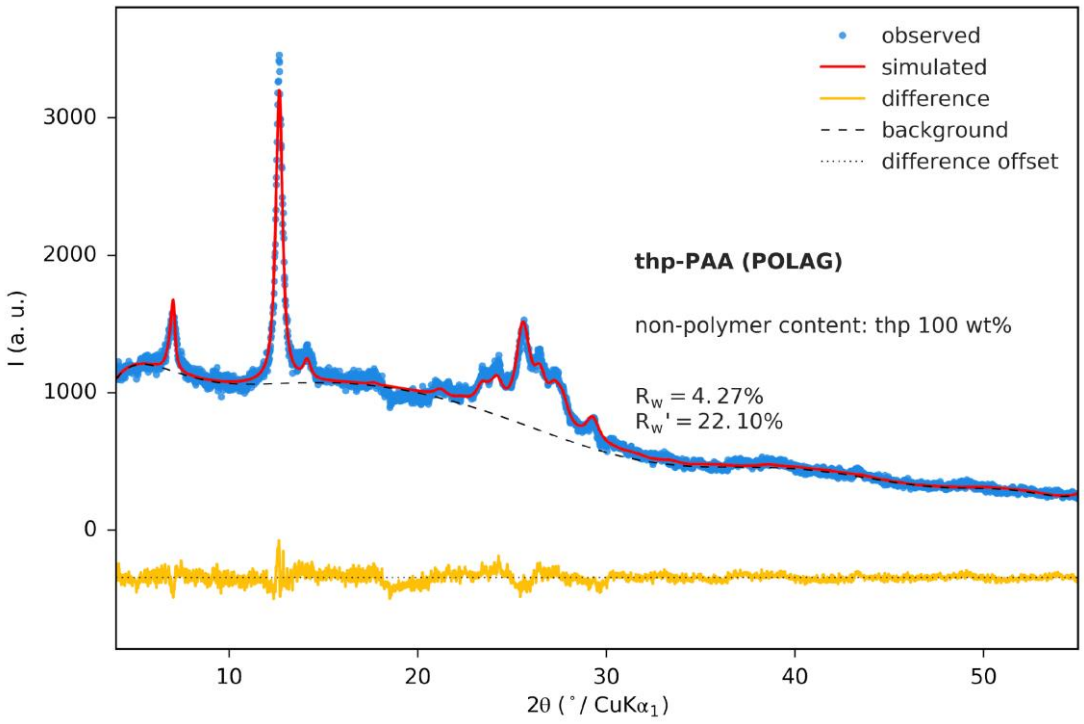

Figure S18: Rietveld refinement of the crystal structure of **thp** to the POLAG sample of **thp**-PAA.

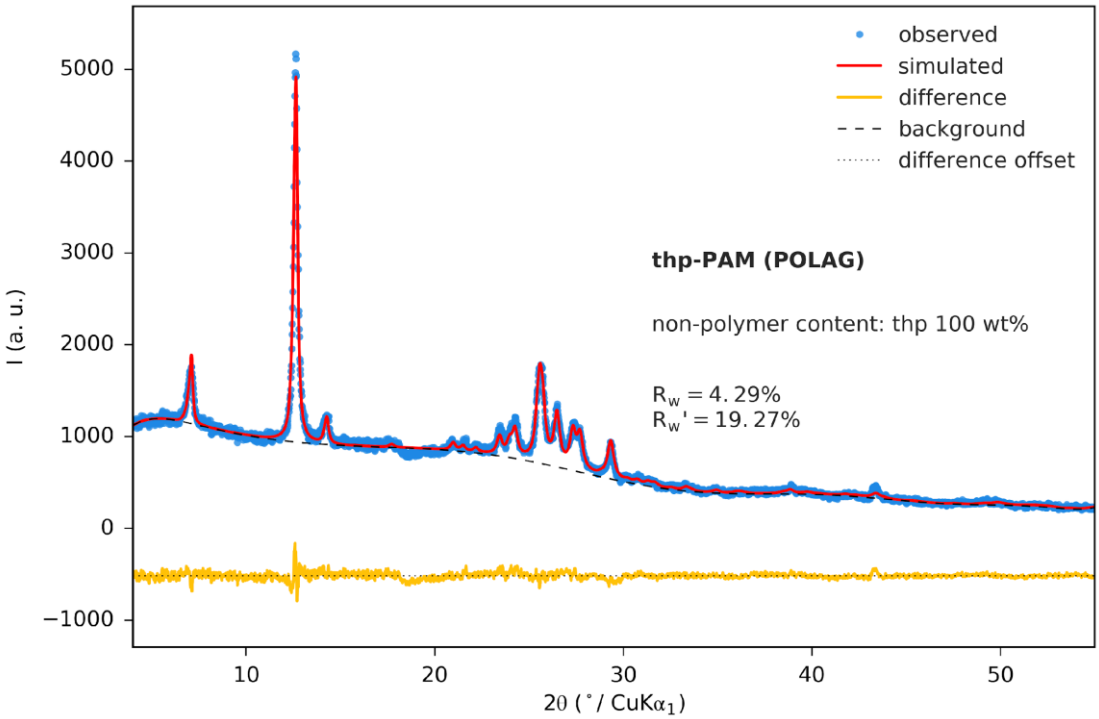

Figure S19: Rietveld refinement of the crystal structure of **thp** to the POLAG sample of **thp**-PAM.

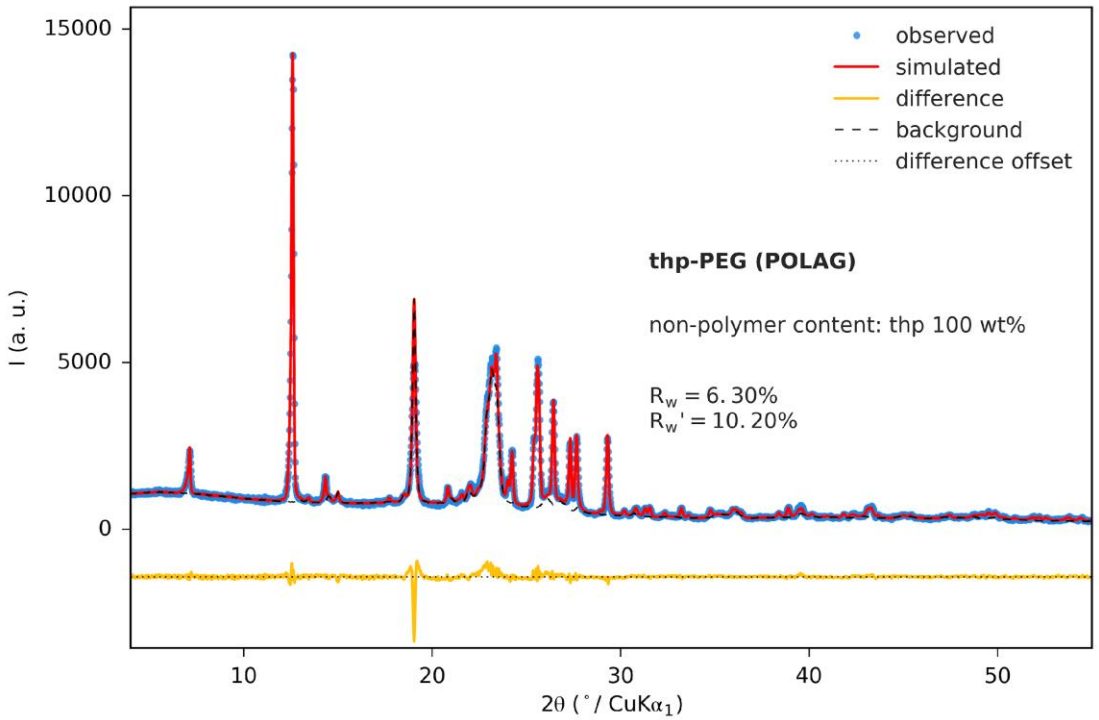

Figure S20: Rietveld refinement of the crystal structure of **thp** to the POLAG sample of **thp**-PEG. The contribution of PEG was modeled by a measurement of pure PEG and included in the background.

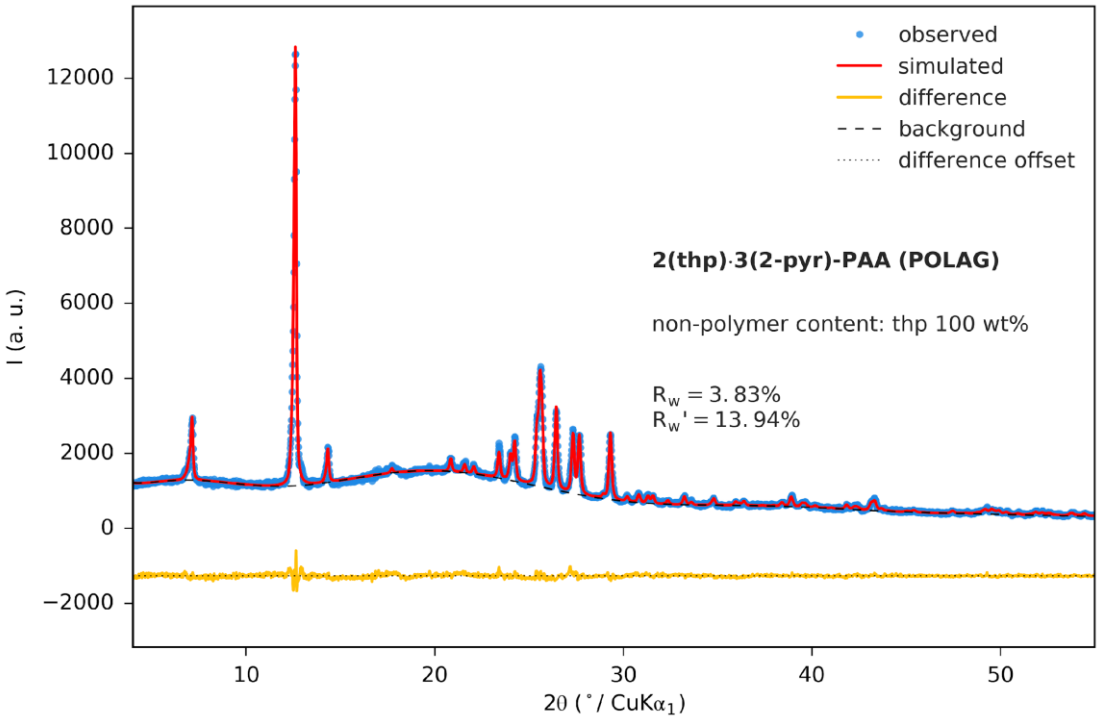

Figure S21: Rietveld refinement of the crystal structure of **thp** to the POLAG sample of sesquisolvate-PAA.

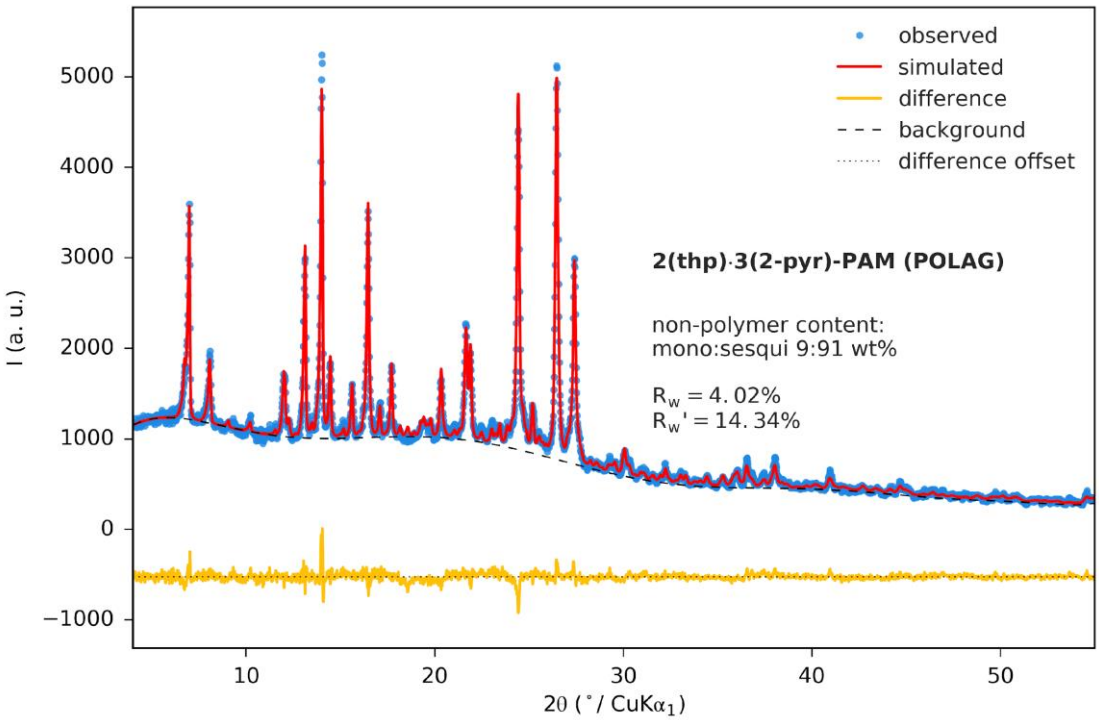

Figure S22: Multiphase Rietveld refinement of the crystal structurse of **thp**:**2-pyr** monosolvate (**mono**) and **thp**:**2-pyr** sesquisolvate (**sesqui**) to the POLAG sample of **sesqui**-PAM.

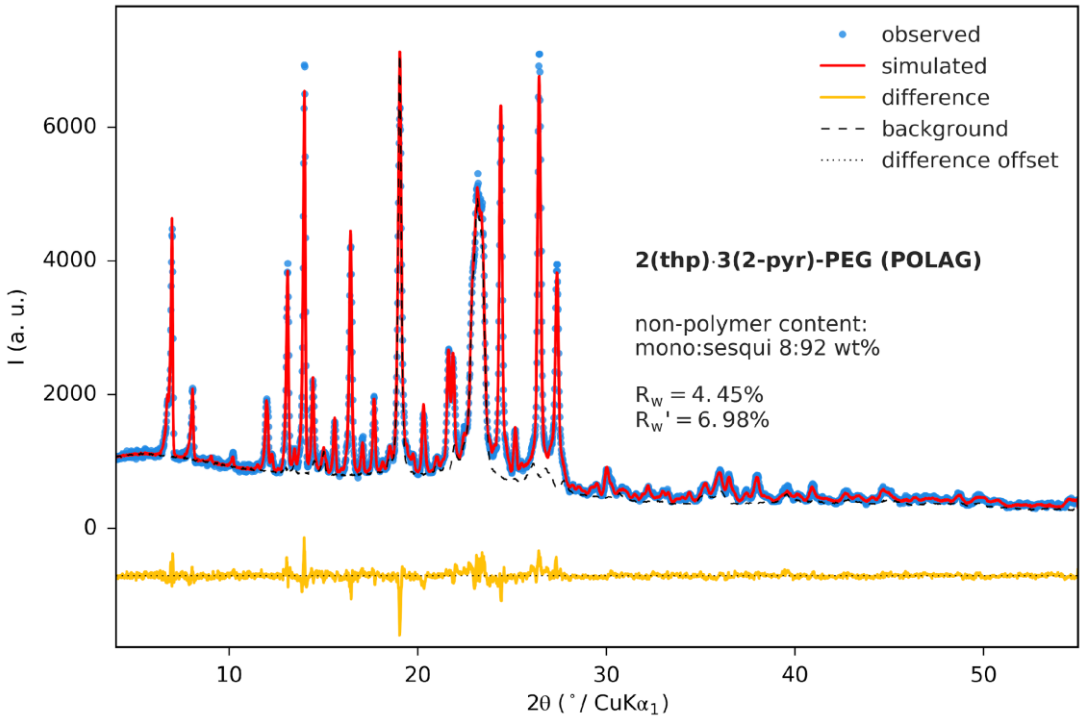

Figure S23: Multiphase Rietveld refinement of the crystal structurse of **thp**:**2-pyr** monosolvate (**mono**) and **thp**:**2-pyr** sesquisolvate (**sesqui**) to the POLAG sample of **sesqui**-PEG. The contribution of PEG was modeled by a measurement of pure PEG and included in the background.

Table S1: Phase and structure details from Rietveld refinements in Figures S13-S21.

Sample	2(**thp**)·3(**2-pyr**)	(**thp**)·(**2-pyr**)	**thp**	**thp**-PAA	**thp**-PAM	**thp**-PEG	2(**thp**)·3(**2-pyr**)-PAA	2(**thp**)·3(**2-pyr**)-PAM	2(**thp**)·3(**2-pyr**)-PEG
Phase 1	2(**thp**)·3(**2-pyr**)	(**thp**)·(**2-pyr**)	**thp**	**thp**	**thp**	**thp**	**thp**	2(**thp**)·3(**2-pyr**)	2(**thp**)·3(**2-pyr**)
Wt%	100	83	100	100	100	100	100	91	92
Space group	$P21/n$	$P\bar{1}$	$Pna21$	$Pna21$	$Pna21$	$Pna21$	$Pna21$	$P21/n$	$P21/n$
Lattice parameters (Å)	a = 7.67 b = 25.21 c = 15.31 β = 92.70	a = 6.79 b = 8.78 c = 11.02 α =82.75 β = 84.81 γ = 81.88	a = 24.62 b = 3.84 c = 8.50	a = 24.96 b = 3.84 c = 8.39	a = 24.70 b = 3.83 c = 8.45	a = 24.65 b = 3.84 c = 8.51	a = 24.64 b = 3.84 c = 8.50	a = 7.67 b = 25.22 c = 15.31 β = 92.72	a = 7.68 b = 25.25 c = 15.33 β = 92.72
Phase 2	–	2(**thp**)·3(**2-pyr**)	–	–	–	–	–	(**thp**)·(**2-pyr**)	(**thp**)·(**2-pyr**)
Wt%	–	17	–	–	–	–	–	9	8
Space group	–	$P21/n$	–	–	–	–	–	$P\bar{1}$	$P\bar{1}$
Lattice parameters (Å)	–	a = 7.67 b = 25.22 c = 15.31 β = 92.69	–	–	–	–	–	a = 6.79 b = 8.79 c = 11.02 α = 82.69 β = 84.87 γ =81.93	a = 6.80 b = 8.80 c = 11.04 α = 82.87 β = 84.92 γ =81.91
R_w (%)	6.43	9.03	8.93	4.27	4.29	6.30	3.83	4.02	4.45
R_w' (%)	11.70	15.20	15.03	22.10	19.27	10.20	13.94	14.34	6.98

4.4. Total scattering data and analysis

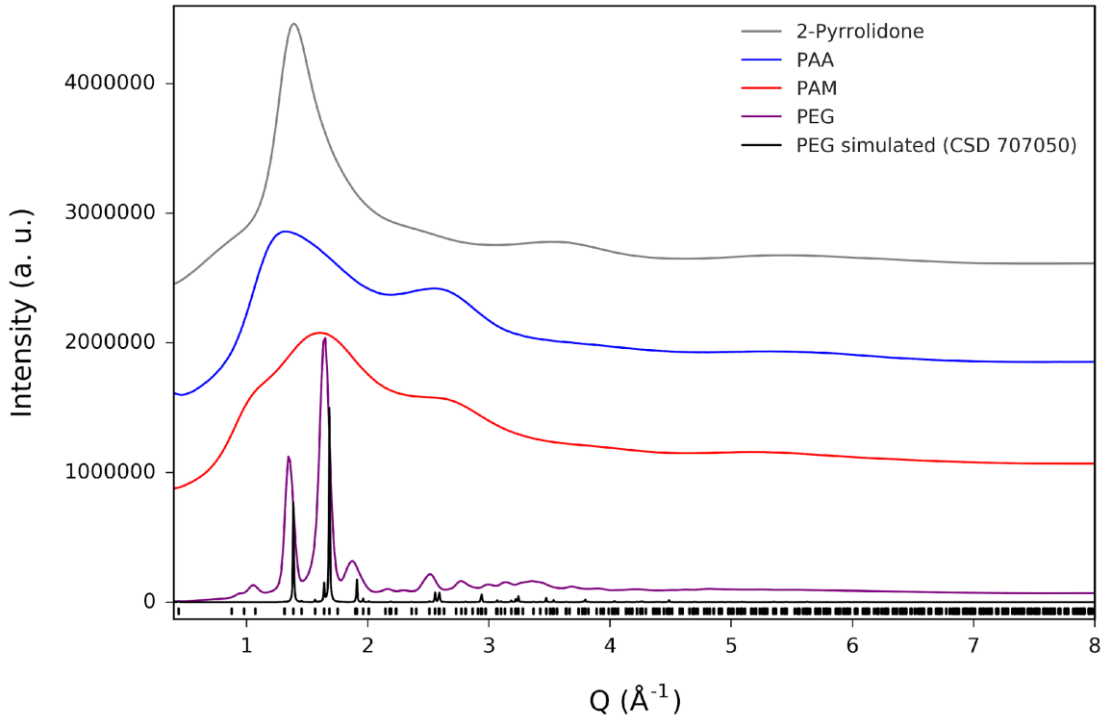

Figure S24: High-energy XRPD patterns (background subtracted, rescaled, and offset from one another) measured from solvent and polymer samples.

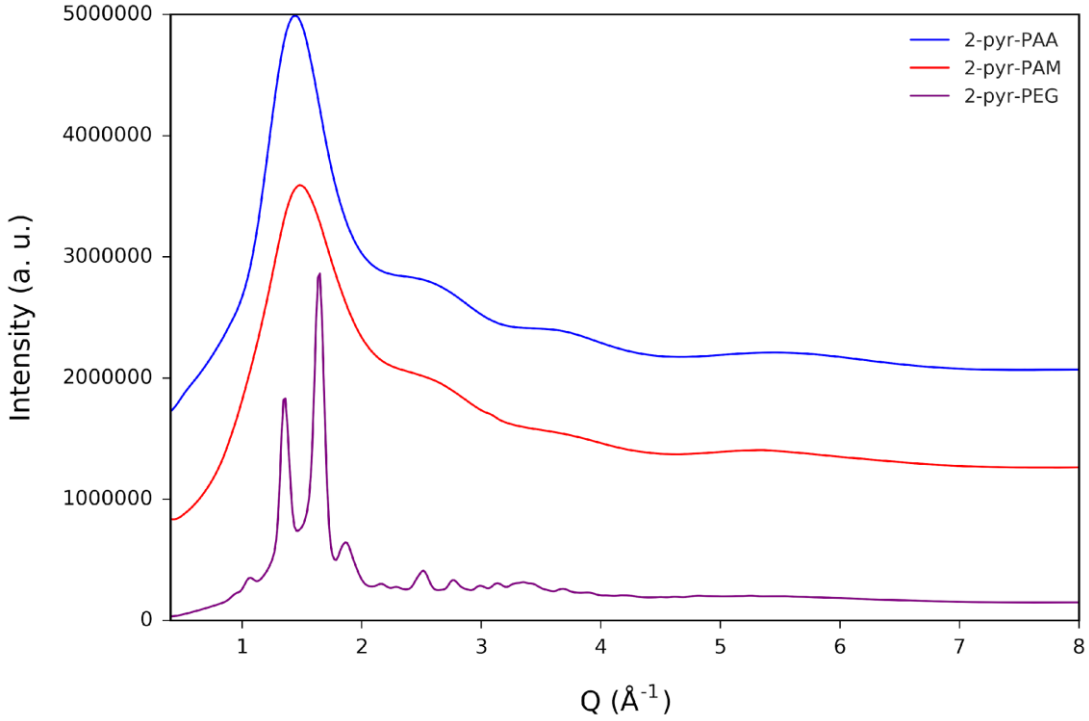

Figure S25: High-energy XRPD patterns (background subtracted, rescaled, and offset from one another) measured from POLAG mixtures of 2-pyr with PAA, PAM, and PEG.

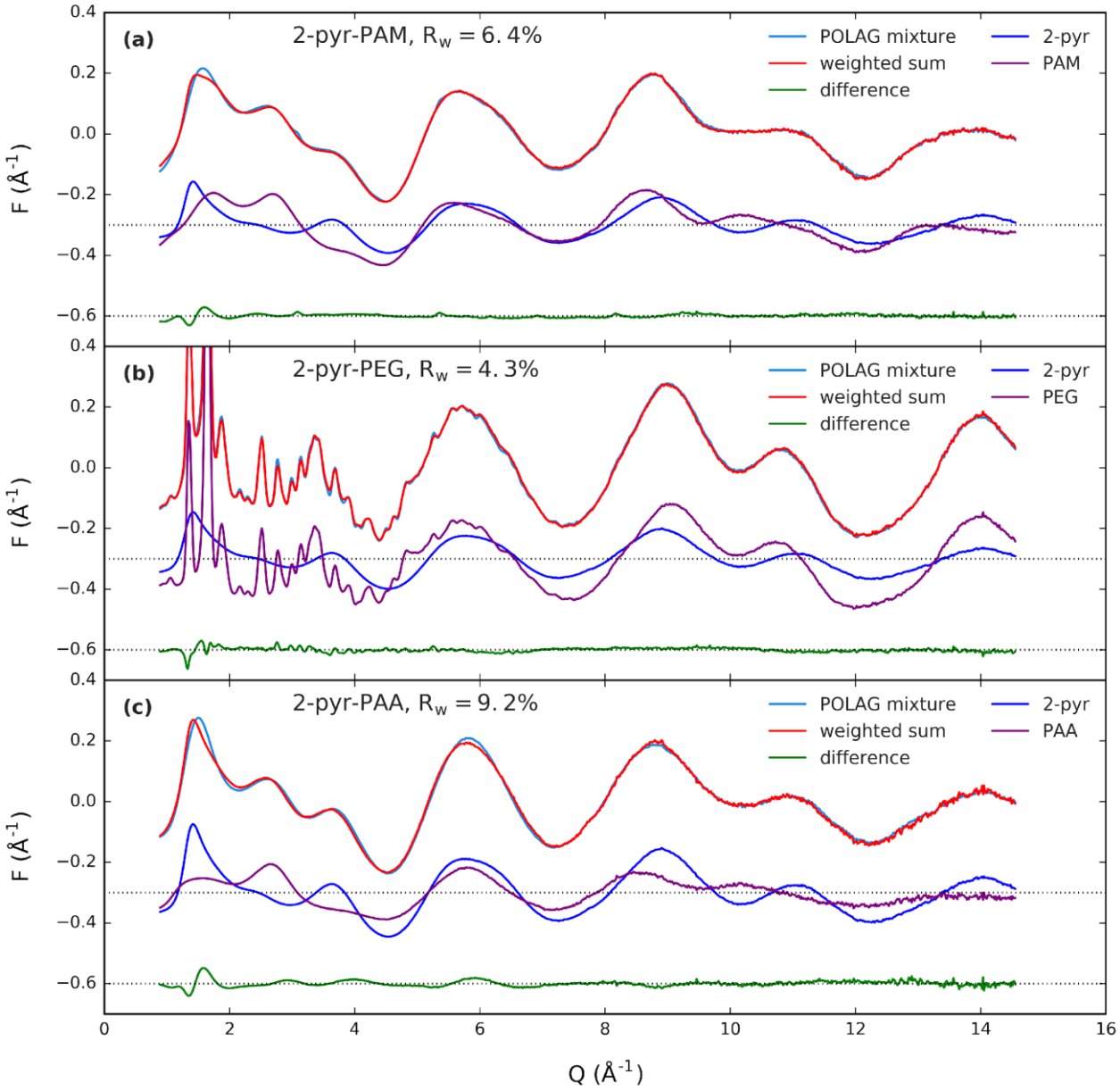

Figure S26: Fits to the reduced total scattering functions $F(Q)$'s of the binary mixtures of (a) **2-pyr**-PAM, (b) **2-pyr**-PEG, (c) **2-pyr**-PAA, using a weighted sum of the pure component patterns. The best fit for PEG is due to the fit of the Bragg peaks from the PEG phase, making this fit less sensitive to small differences in the amorphous component. For PAA and PAM, the first sharp diffraction peak is poorly fit indicating changes in intermediate range order. For PAA, more significant misfit is present at higher-Q values indicating more coherent local structure changes.

4.5. PDF analysis

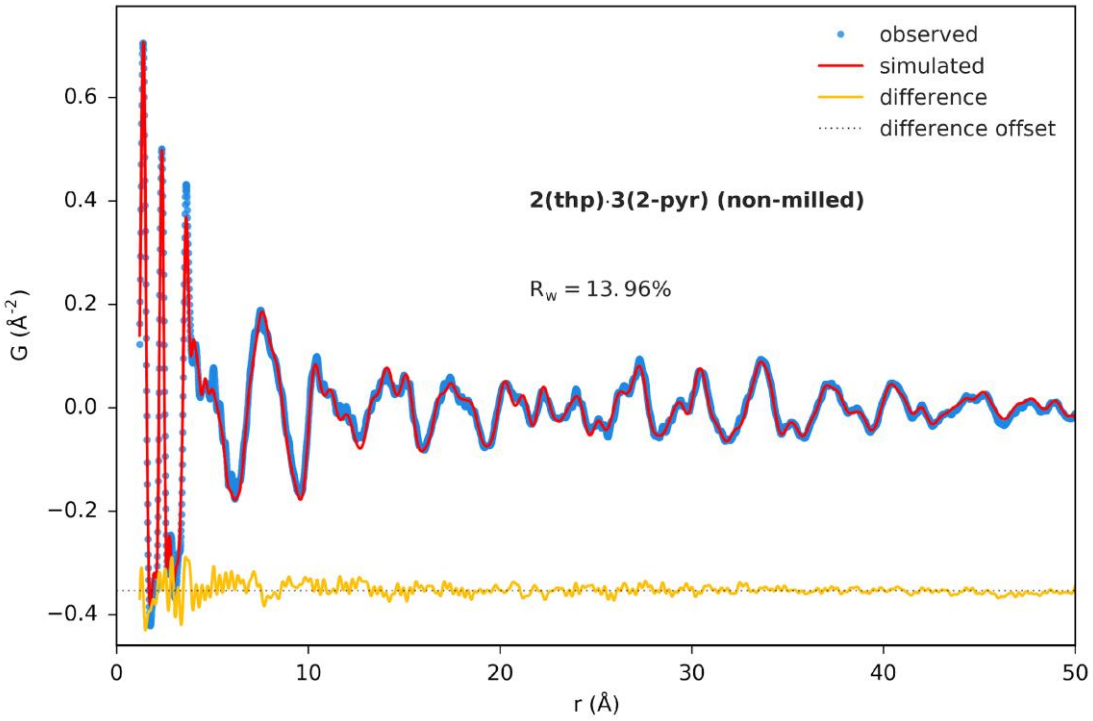

Figure S27: Fit resulting from real-space structure refinement of the **thp**:**2-pyr** sesquisolvate crystal structure to the measured PDF of the non-milled **thp**:**2-pyr** sesquisolvate sample.

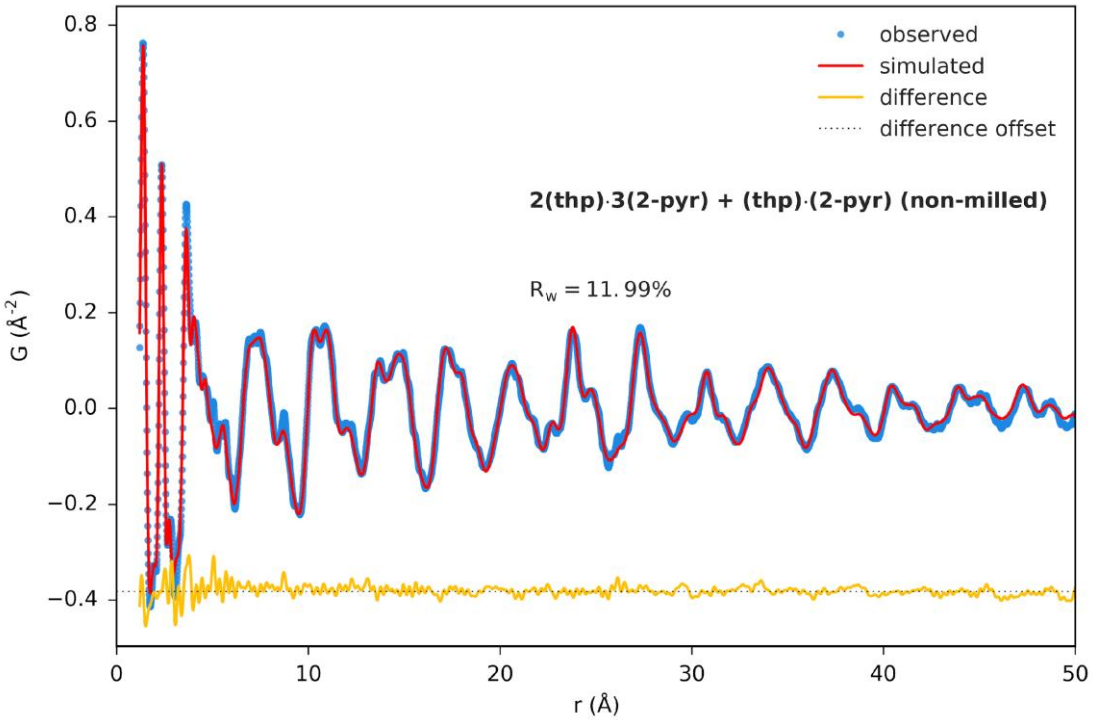

Figure S28: Fit resulting from multiphase**,** real-space structure refinement of **thp**:**2-pyr** sesquisolvate plus **thp**:**2-pyr** monosolvate crystal structure to the measured PDF of non-milled **thp**:**2-pyr** monosolvate sample.

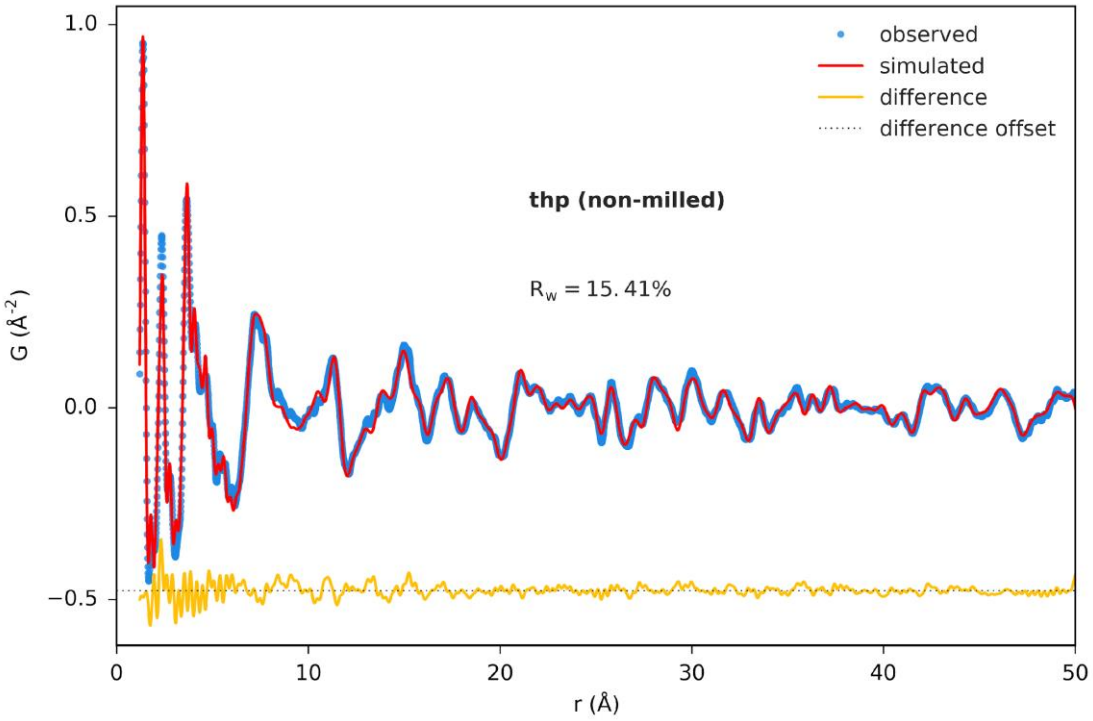

Figure S29: Fit resulting from real-space structure refinement of the **thp** crystal structure (form II) to the measured PDF of the non-milled **thp** sample.

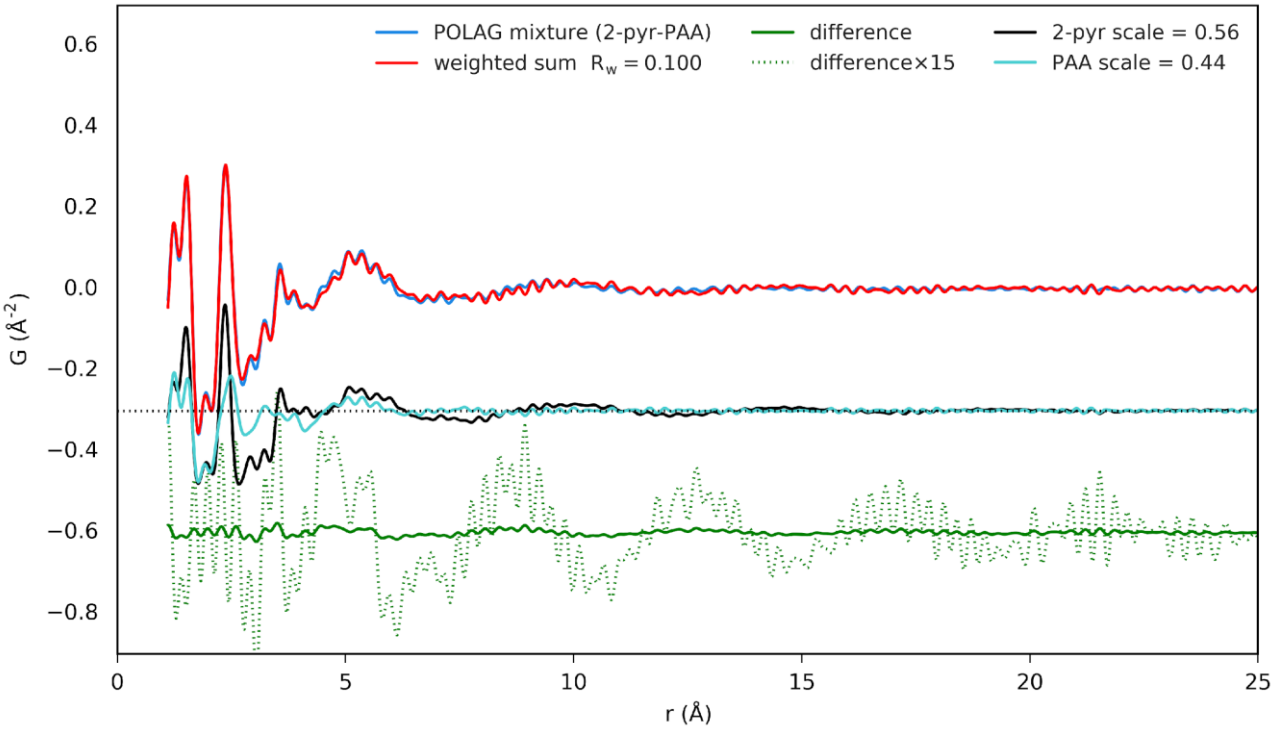

Figure S30: Pattern indexing of the PDF from the POLAG mixture of **2-pyr**-PAA using the measured PDFs of the pure components of **2-pyr** and PAA.

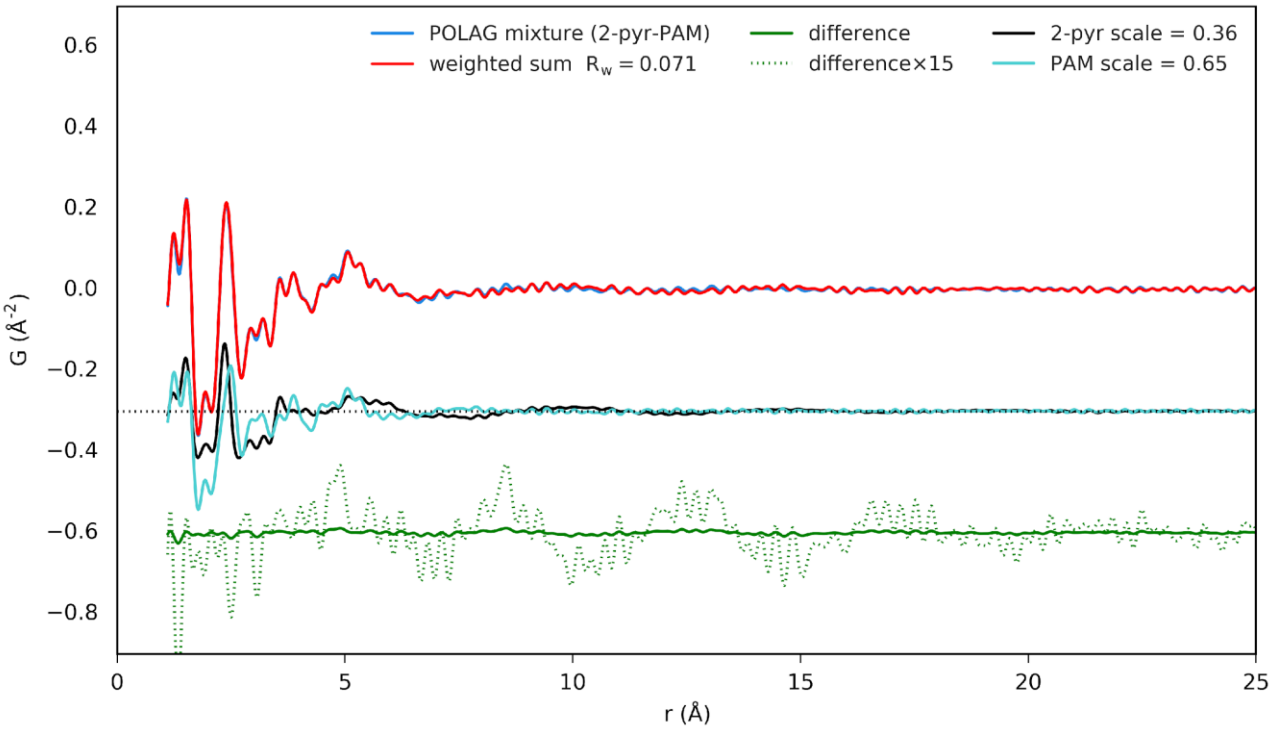

Figure S31: Pattern indexing of the PDF from the POLAG mixture of **2-pyr**-PAM using the measured PDFs of the pure components of **2-pyr** and PAM.

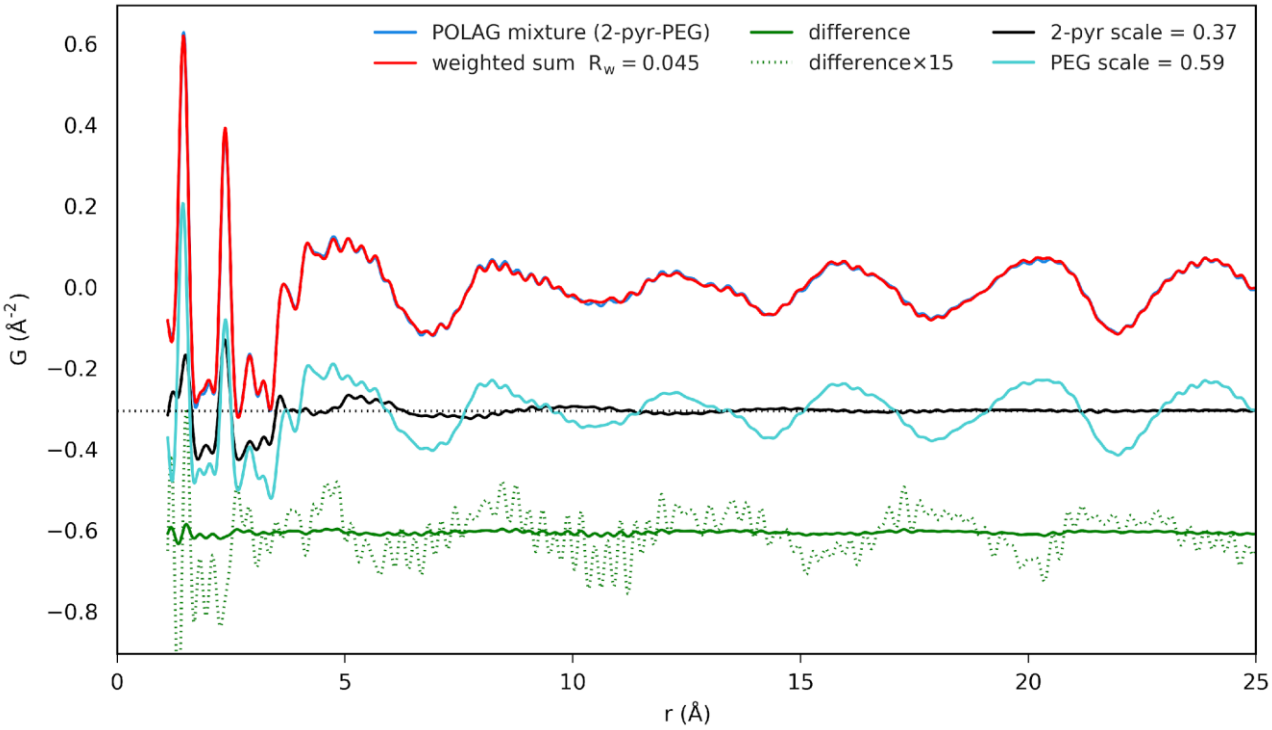

Figure S32: Pattern indexing of the PDF from the POLAG mixture of **2-pyr**-PEG using the measured PDFs of the pure components of **2-pyr** and PEG.

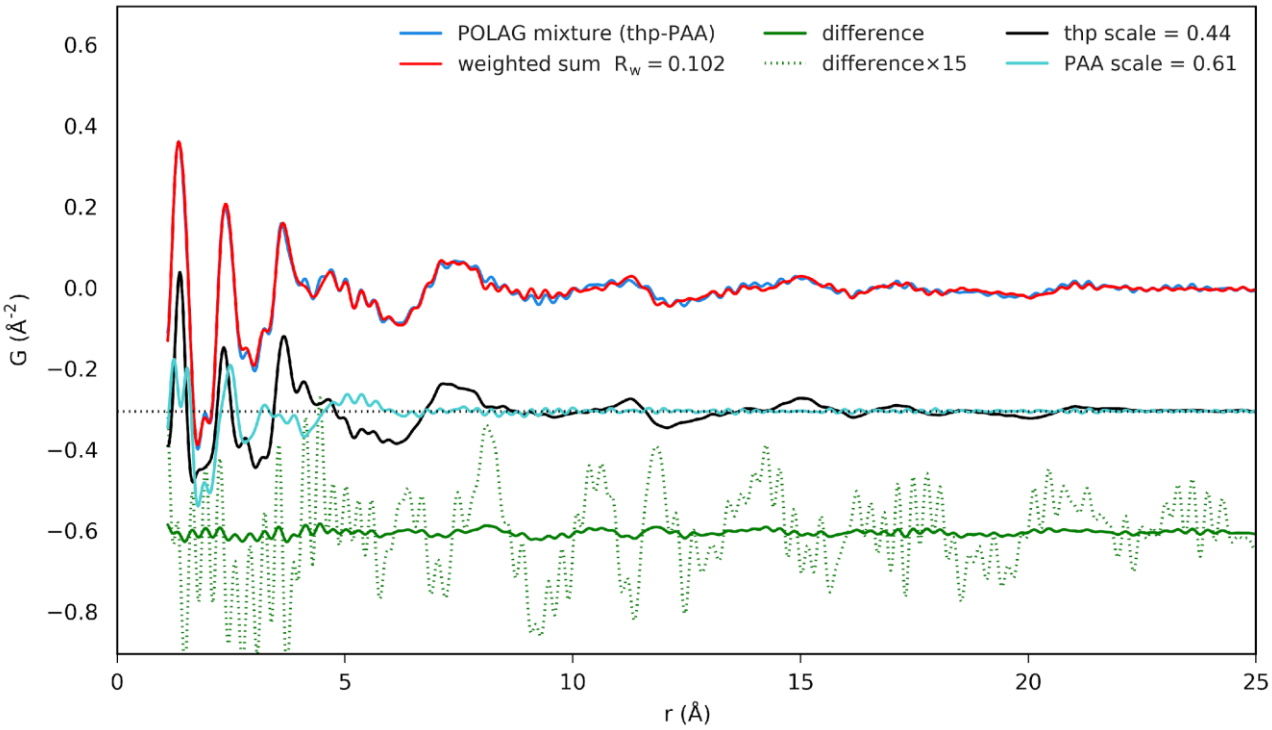

Figure S33: Pattern indexing of the PDF from the POLAG mixture of **thp**-PAA using the measured PDFs of the pure components of **thp** and PAA.

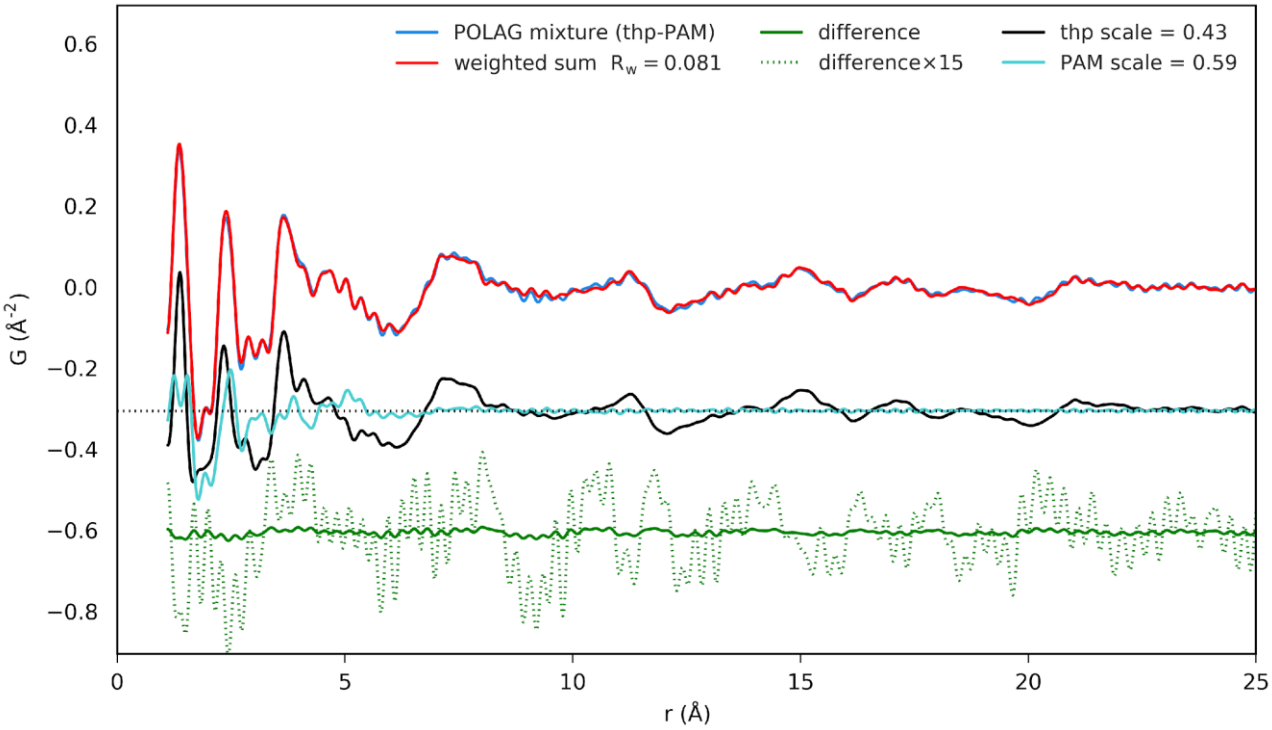

Figure S34: Pattern indexing of the PDF from the POLAG mixture of **thp**-PAM using the measured PDFs of the pure components of **thp** and PAM.

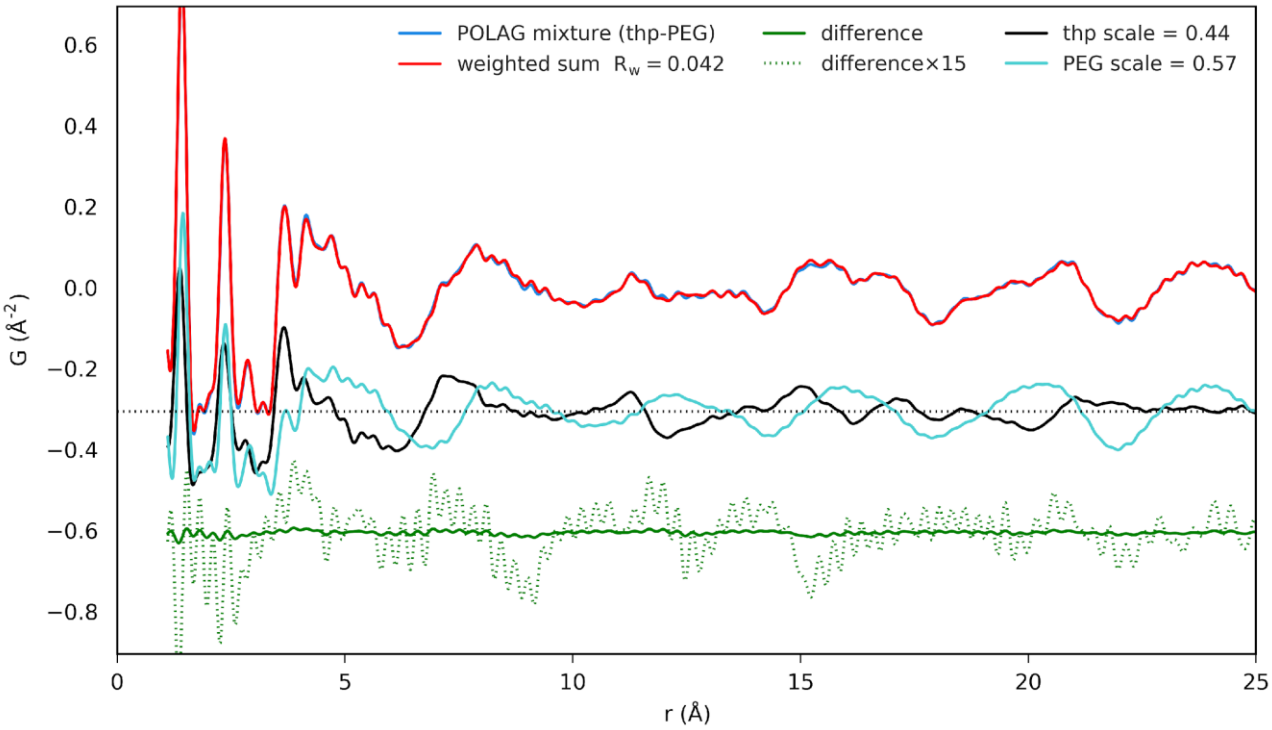

Figure S35: Pattern indexing of the PDF from the POLAG mixture of **thp**-PEG using the measured PDFs of the pure components of **thp** and PEG.

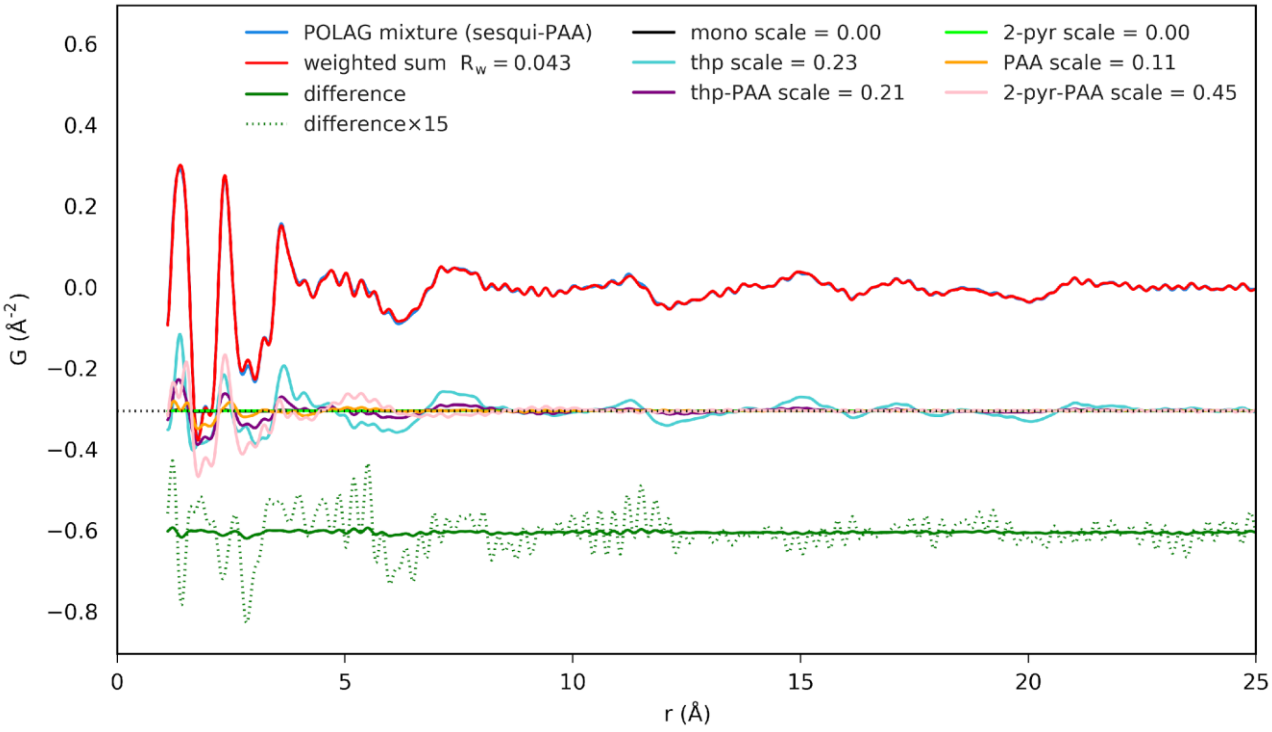

Figure S36: Pattern indexing of the PDF from the POLAG mixture of **thp**:**2-pyr** sesquisolvate (**sesqui**)-PAA using the measured PDFs of the pure components and the binary mixtures.

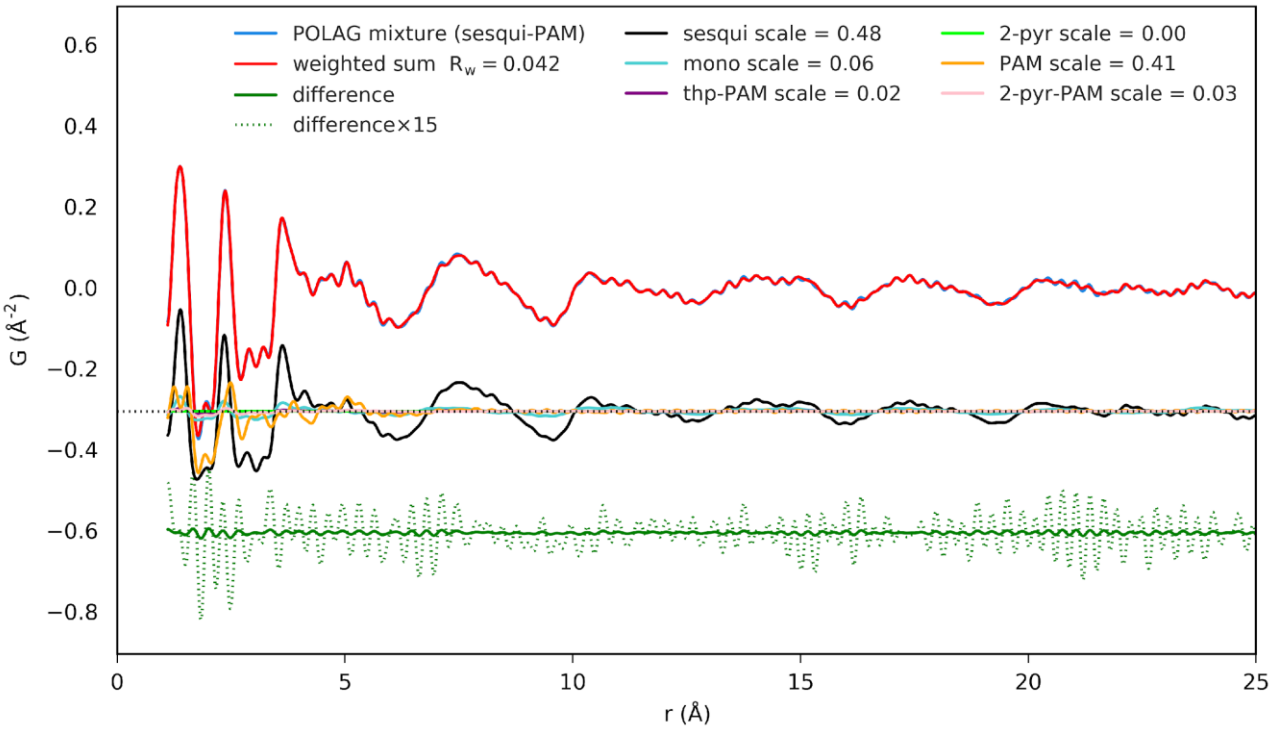

Figure S37: Pattern indexing of the PDF from the POLAG mixture of **thp**:**2-pyr** sesquisolvate (**sesqui**)-PAM using the measured PDFs of the pure components and the binary mixtures.

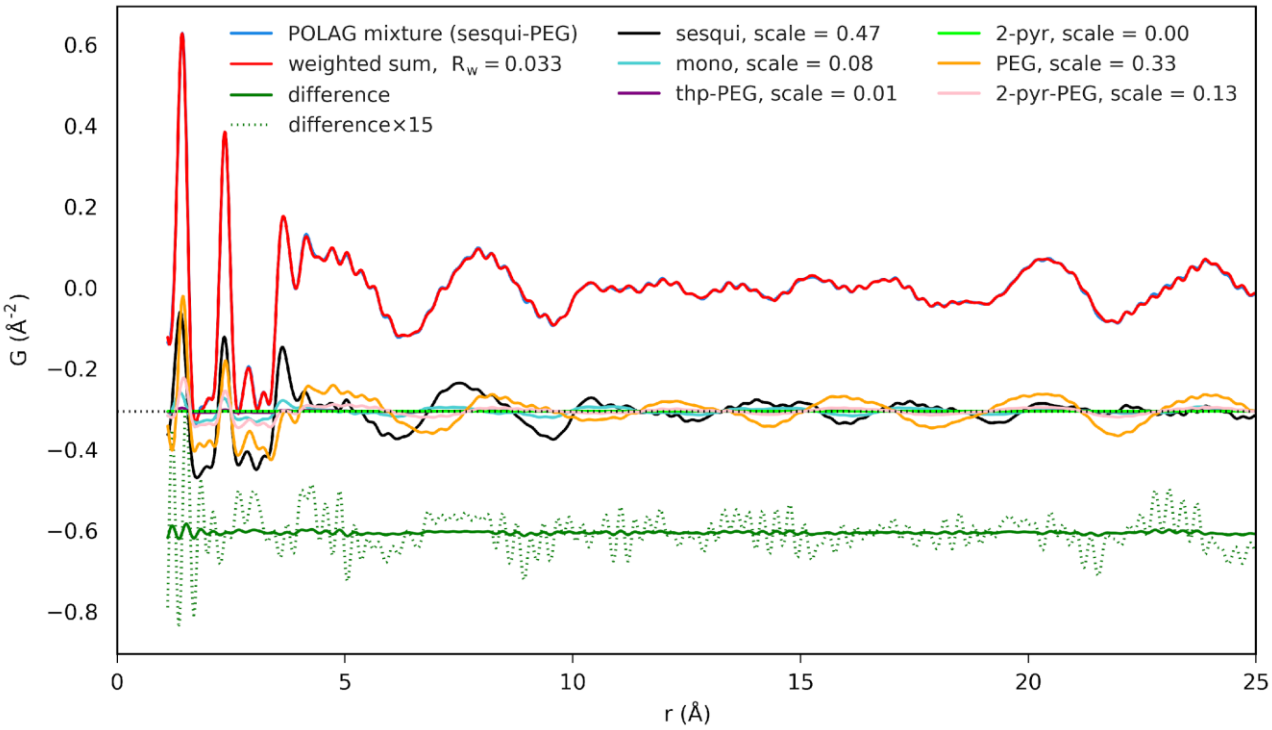

Figure S38: Pattern indexing of the PDF from the POLAG mixture of **thp**:**2-pyr** sesquisolvate (**sesqui**)-PEG using the measured PDFs of the pure components and the binary mixtures.

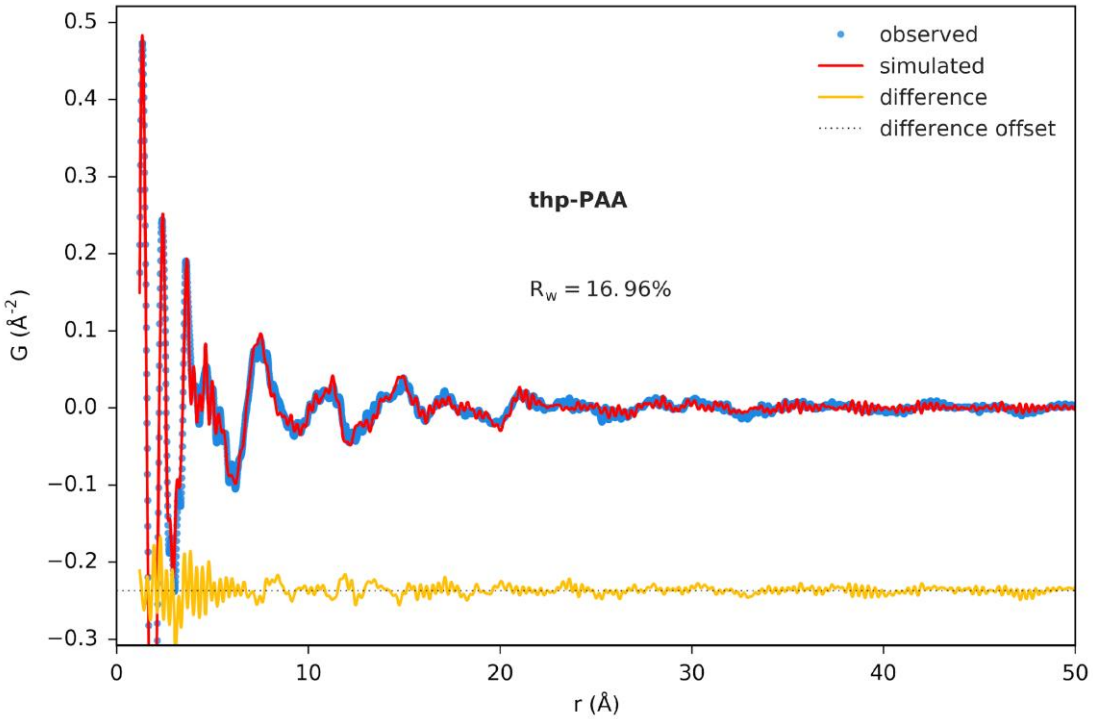

Figure S39: Structure refinement of the **thp** crystal structure to the PDF from the POLAG mixture of **thp**-PAA (same sample as in Fig. S31). The polymer contribution is accounted for here by adding the measured pattern of PAA and refining a scale factor.

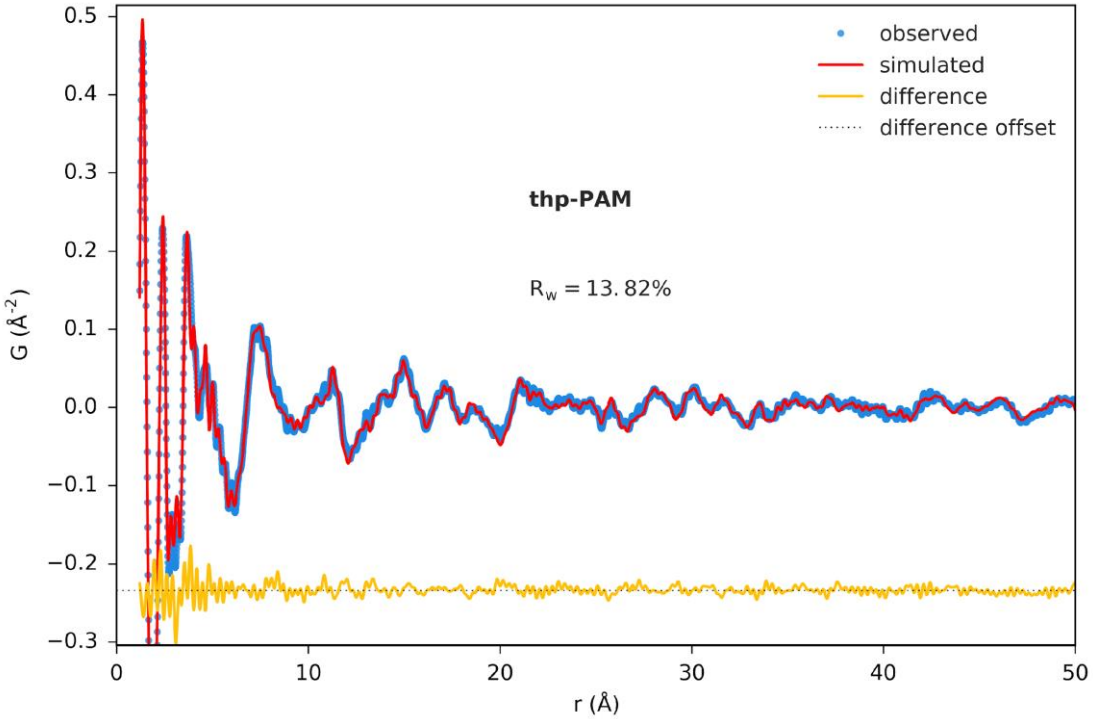

Figure S40: Structure refinement of the **thp** crystal structure to the PDF from the POLAG mixture of **thp**-PAM (same sample as in Fig. S32). The polymer contribution is accounted for here by adding the measured pattern of PAM and refining a scale factor.

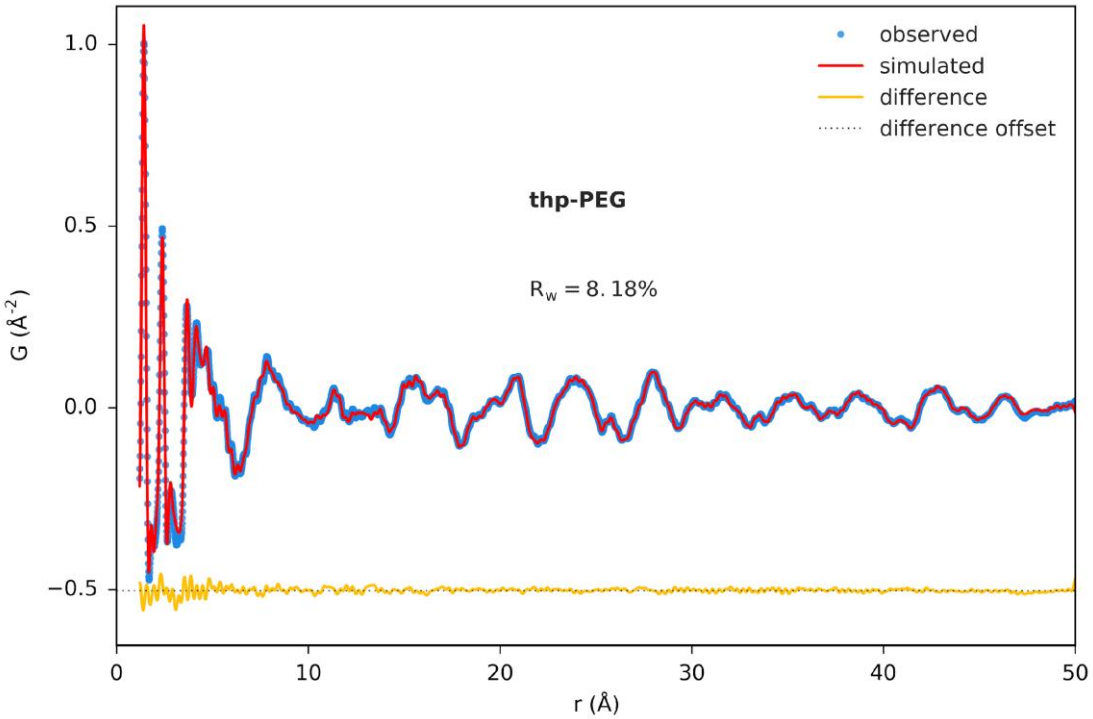

Figure S41: Structure refinement of the **thp** crystal structure to the PDF from the POLAG mixture of **thp**-PEG (same sample as in Fig. S33). The polymer contribution is accounted for here by adding the measured pattern of PEG and refining a scale factor.

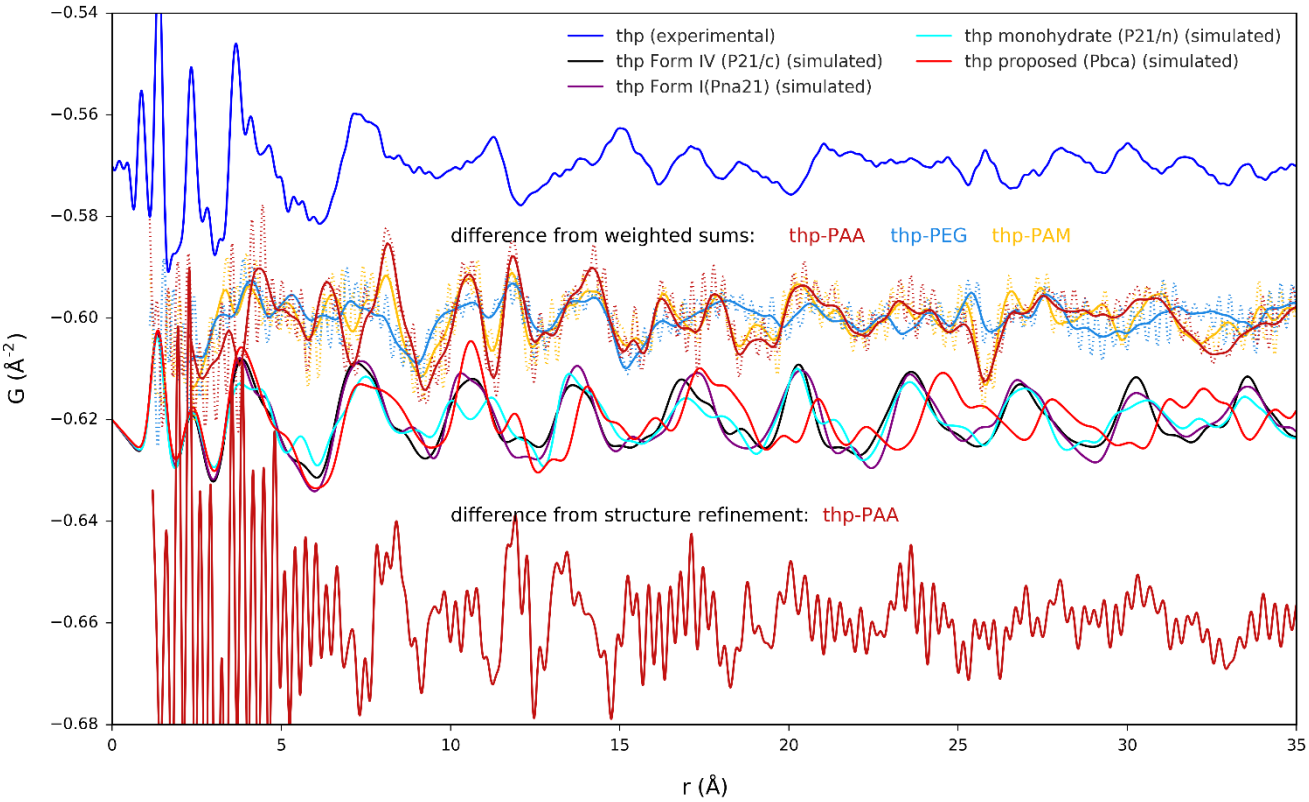

Figure S42: Residuals from the weighted sum fits of **thp** and polymer PDF patterns to those of the POLAG mixtures of **thp**-PAA (Fig. 31), **thp**-PAM (Fig. 32), and **thp**-PEG (Fig. 33) (dotted lines are from fits using a $Q_{max} = 22.5$ Å^{-1} and the solid lines are from fits using $Q_{max} = 15$ Å^{-1}). The blue line offset above the residuals is the measured PDF of non-milled **thp** and the three lines plotted below are the PDFs simulated from the structures of **thp** Forms I, IV, monohydrate, and a proposed structure. These show that the features are not well described by those of a nanostructured form of another known polymorph, which was confirmed by no improvement in Rw achieved by adding these phases to the structure refinement. An additional residual from structure refinement of **thp** crystal structure model plus the polymer pattern to the PDF of **thp**-PAA (Fig. S37) is plotted at the bottom, showing that the residual features are not described by a modified **thp** Form II structure.

4.6. Raman spectroscopy analysis

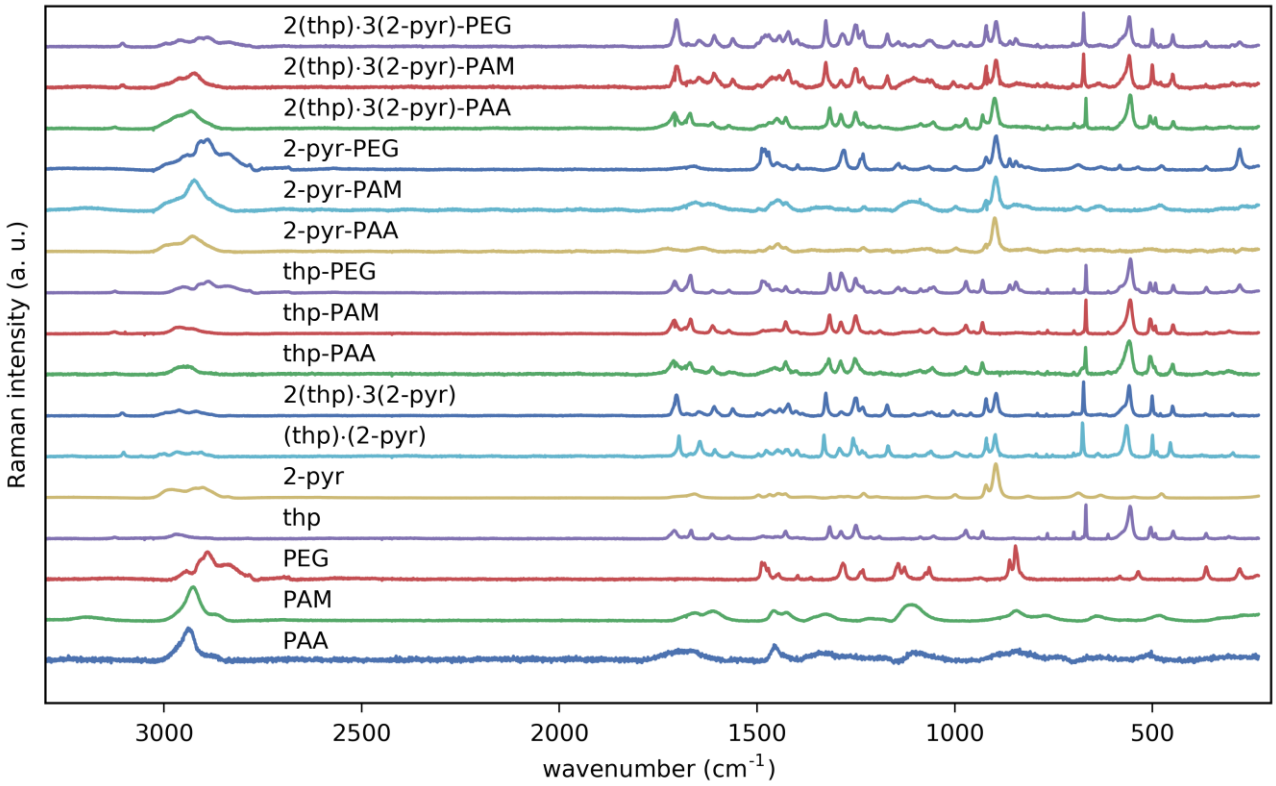

Figure S43: Raman spectra for all samples after background subtraction and normalization by the value of maximum intensity.

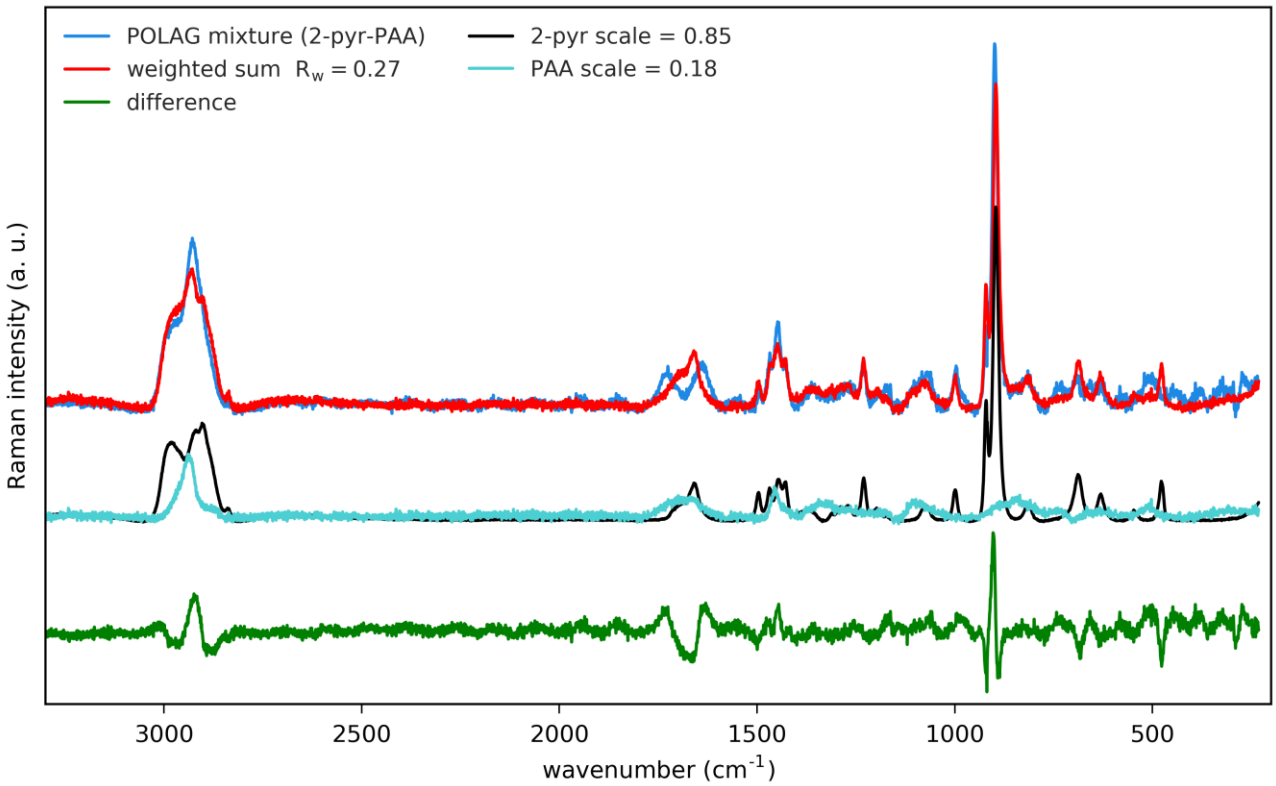

Figure S44: Pattern indexing of the Raman spectrum of the POLAG mixture of **2-pyr**-PAA using the spectra of the pure components. There is a clear modification of the bands spanning 1600–1780 cm^{-1}, which suggests that the pure component interact to give new chemical environments.

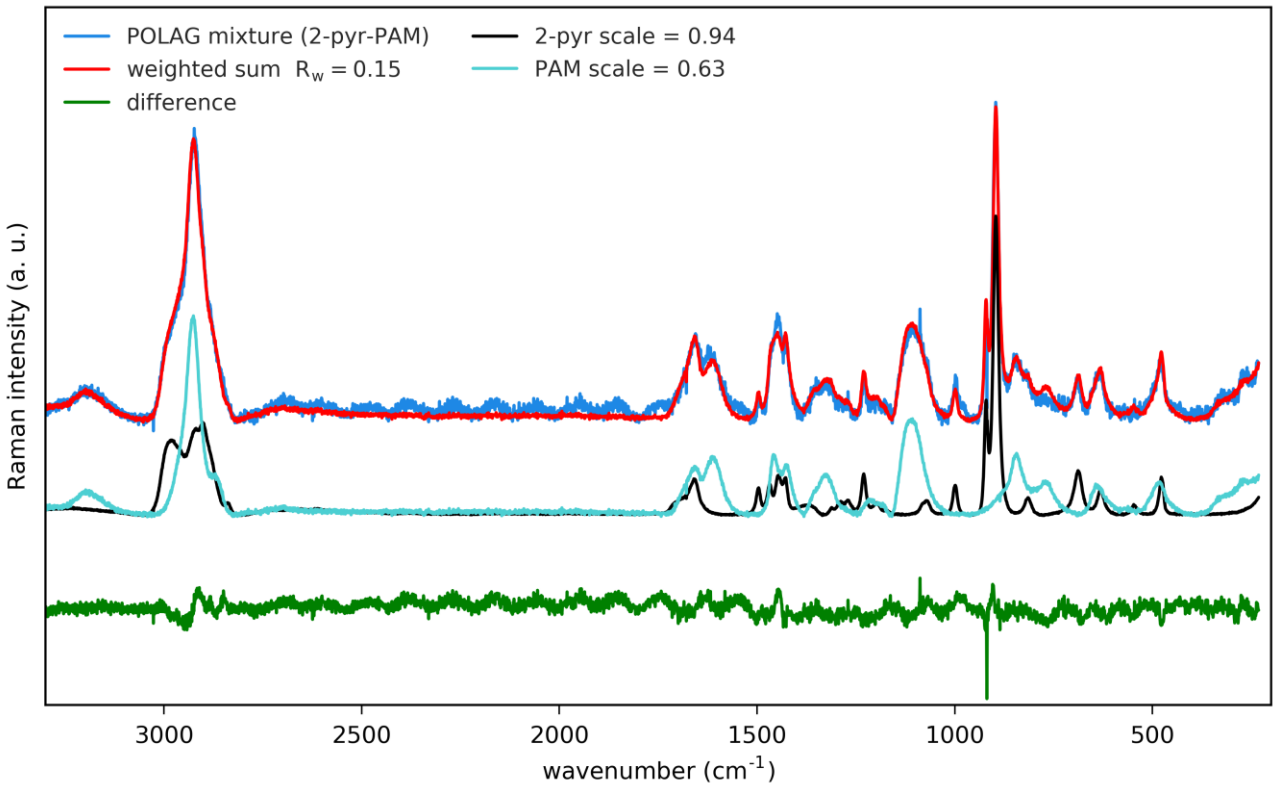

Figure S45: Pattern indexing of the Raman spectrum of the POLAG mixture of **2-pyr**-PAM using the spectra of the pure components. The indexing is quite good without any distinct modifications.

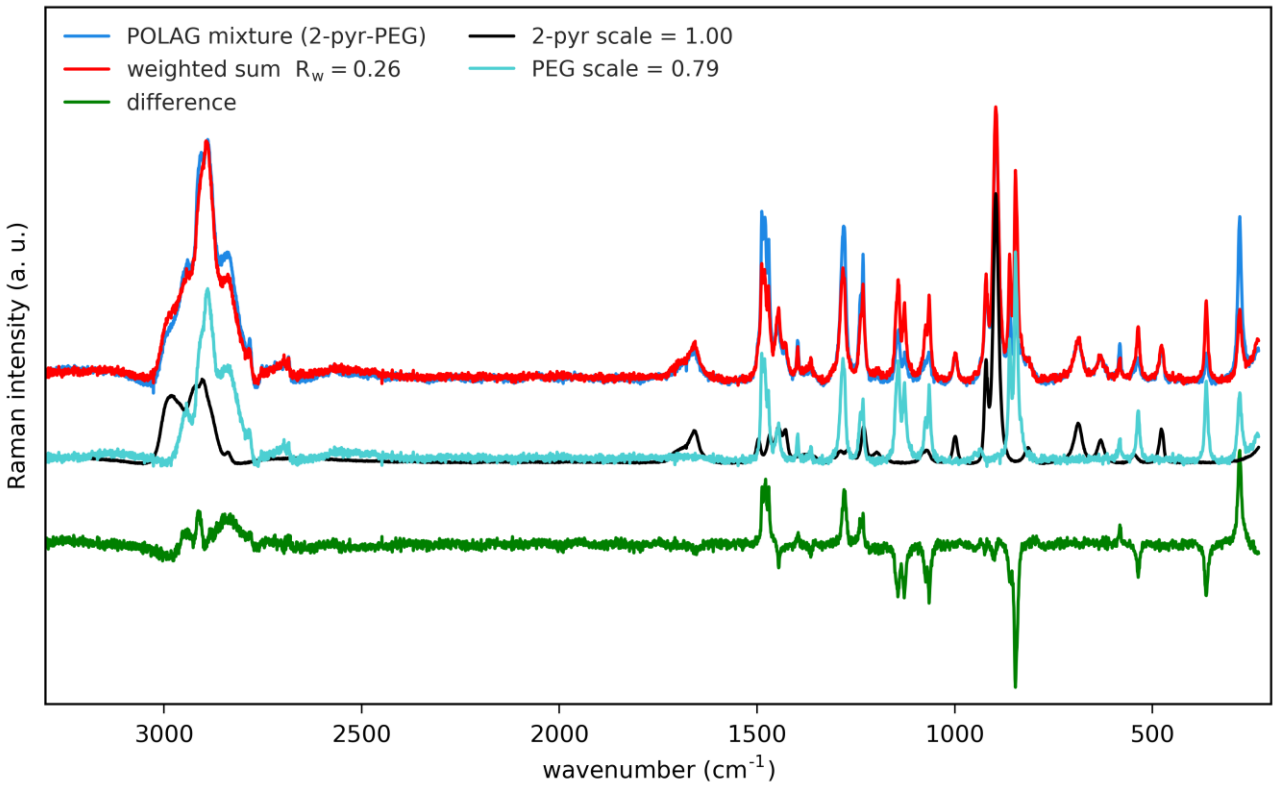

Figure S46: Pattern indexing of the Raman spectrum of the POLAG mixture of **2-pyr**-PEG using the spectra of the pure components. The relative intensities of bands associated with PEG appear to be significantly modified, suggesting structural modification of PEG.

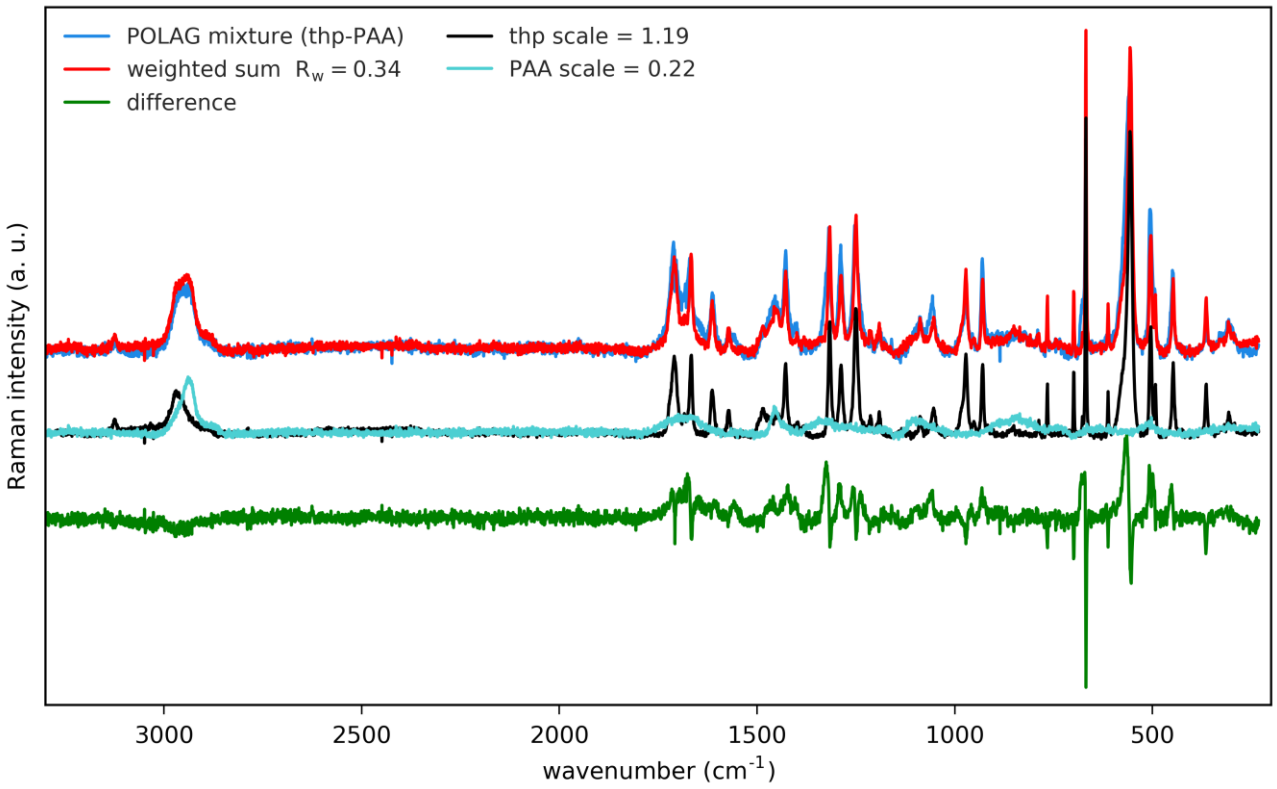

Figure S47: Pattern indexing of the Raman spectrum of the POLAG mixture of **thp**-PAA using the spectra of the pure components. The indexing suggests some modifications to the structure of thp.

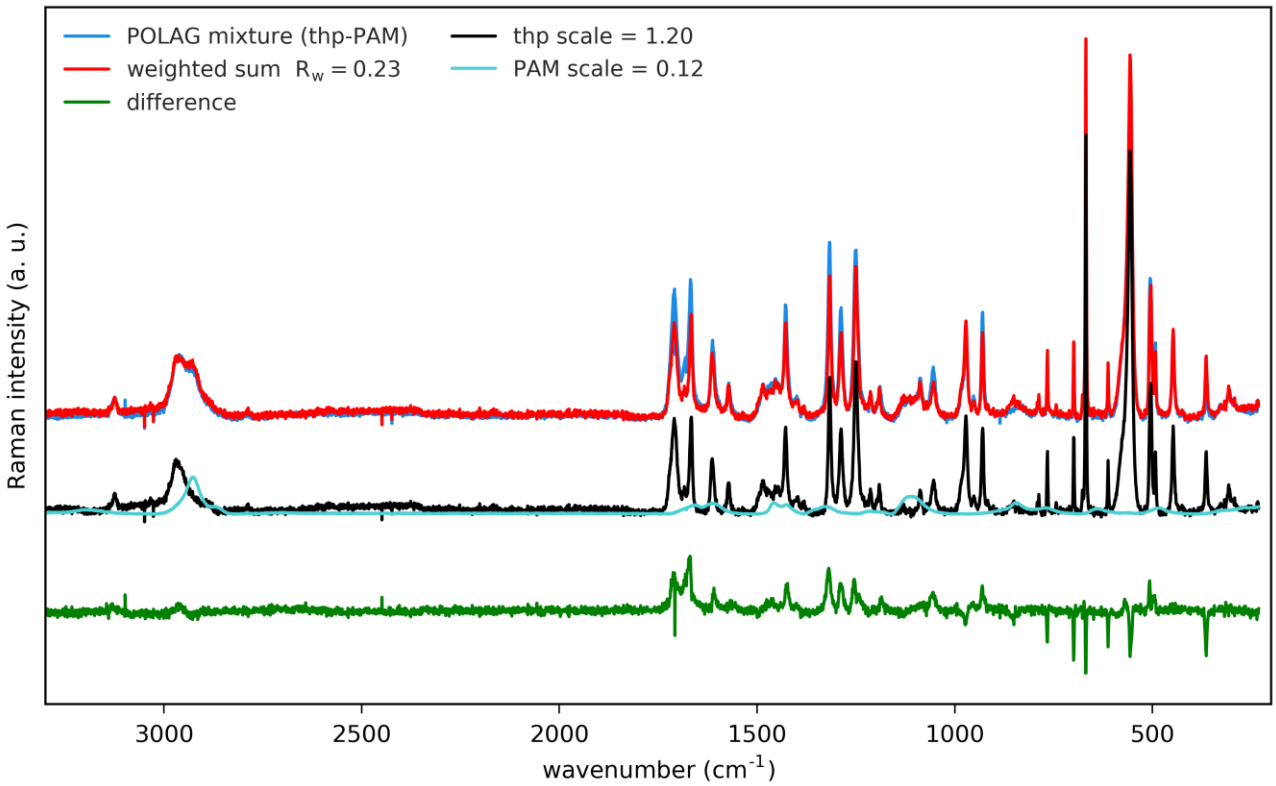

Figure S48: Pattern indexing of the Raman spectrum of the POLAG mixture of **thp**-PAM using the spectra of the pure components. The indexing suggests some modifications to the structure of **thp**.

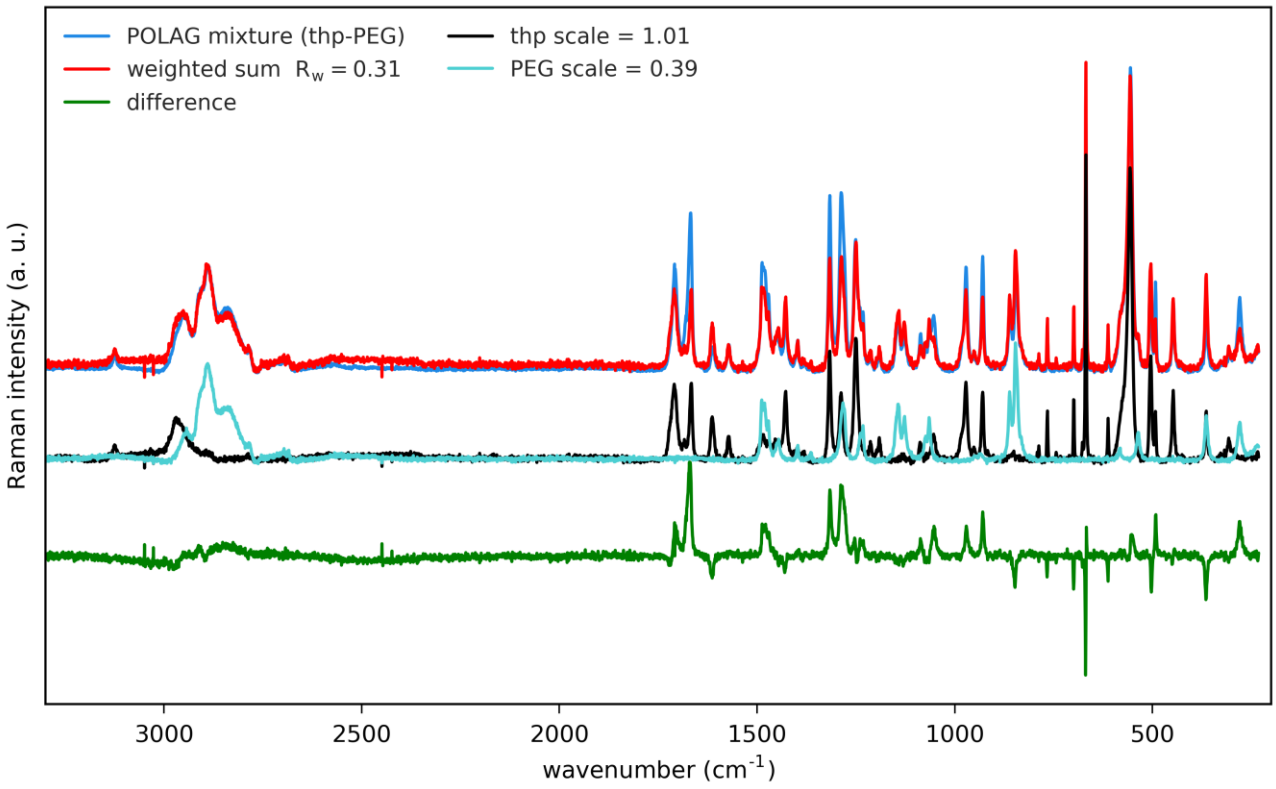

Figure S49: Pattern indexing of the Raman spectrum of the POLAG mixture of **thp**-PEG using the spectra of the pure components. The indexing suggests some modifications to the structure of **thp**.

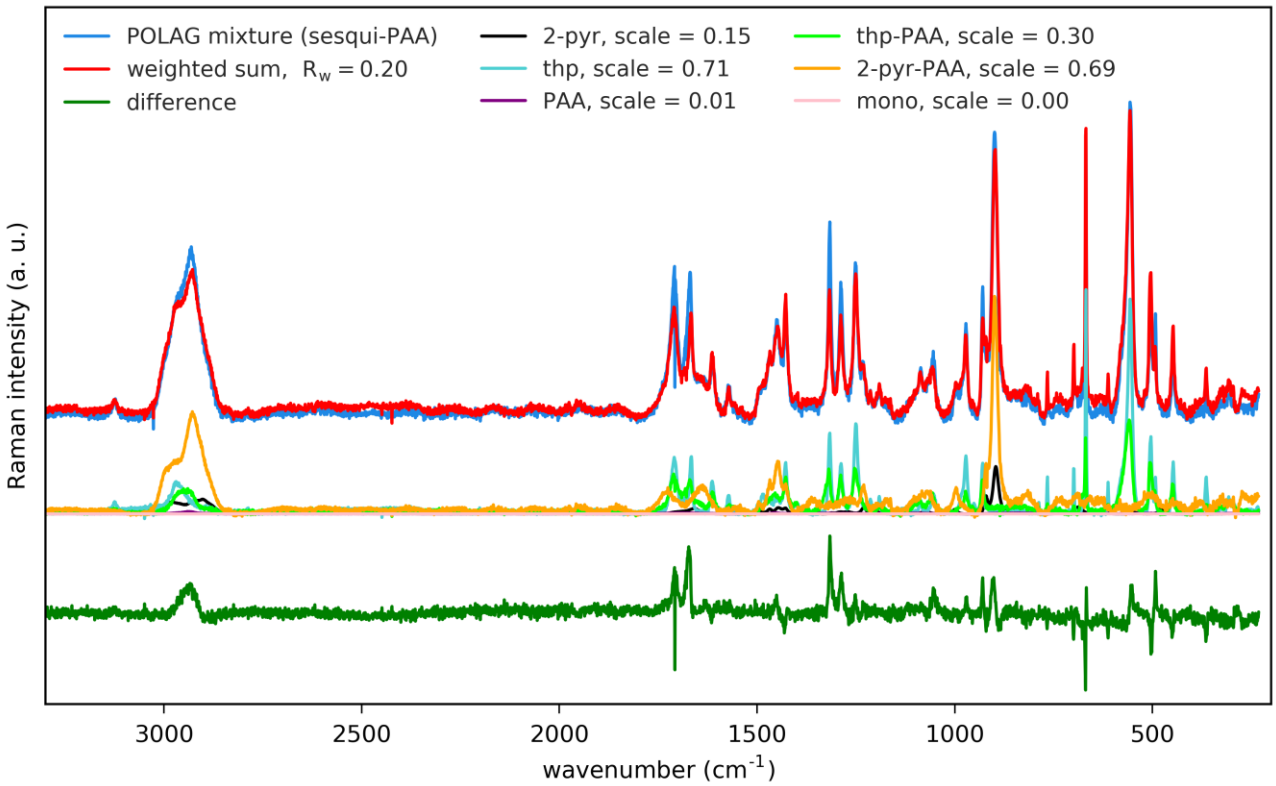

Figure S50: Pattern indexing of the Raman spectrum of the POLAG mixture of **sesqui**-PAA using the spectra of the pure components and binary mixtures. The indexing suggests that the predominant contributions are from **thp**, which was observed to form due to complete desolvation of the sesquisolvate crystal, and to **2-pyr**-PAA, which suggests that PAA takes up and interacts with **2-pyr**. There is also a significant signal from **thp**-PAA, which may suggest either interactions between thp-PAA also occur, or that similar structural modification or degradation of **thp** occurs as in the POLAG sample of thp-PAA. The significance of some pure **2-pyr** is unclear, but may suggest some **2-pyr** extracted has not been incorporated into PAA.

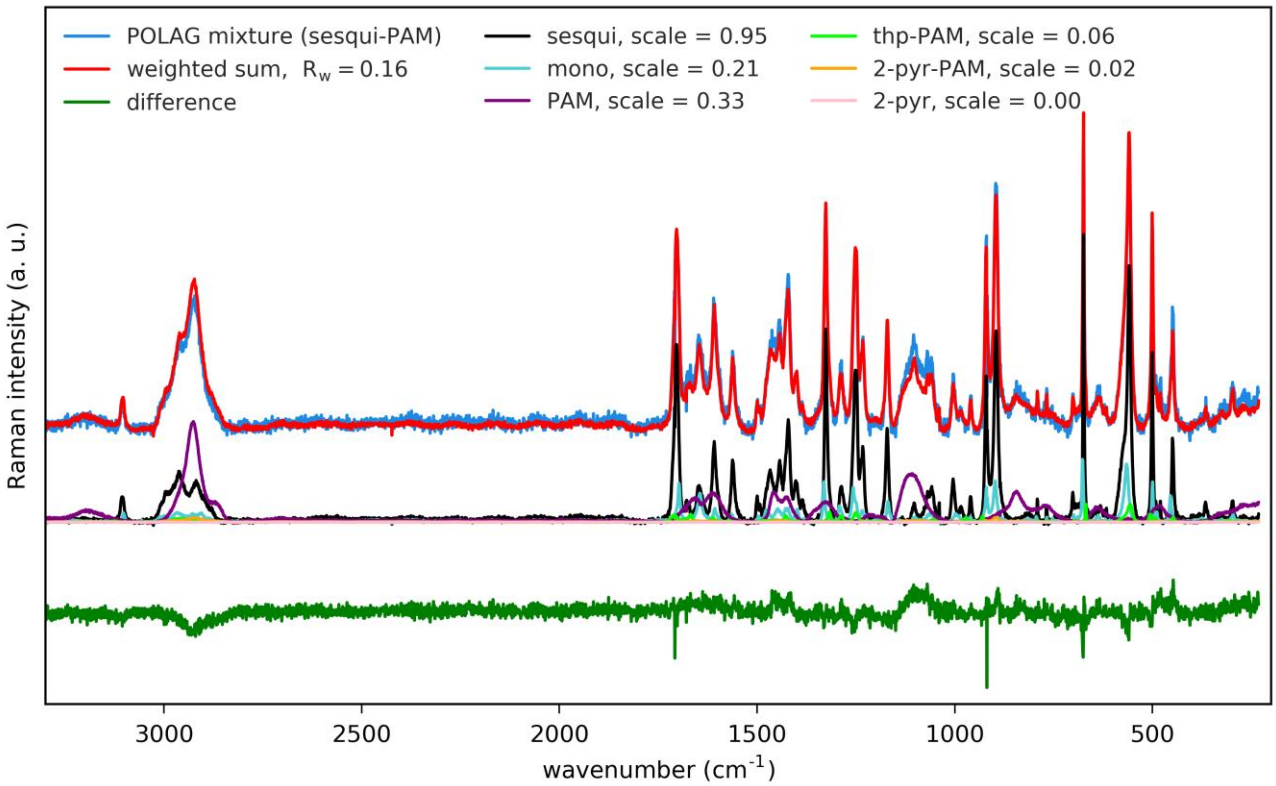

Figure S51: Pattern indexing of the Raman spectrum of the POLAG mixture of **sesqui**-PAM using the spectra of the pure components and binary mixtures. The indexing suggests that the predominant contributions are from **sesqui**, as expected from the XRPD experiments, and the polymer.

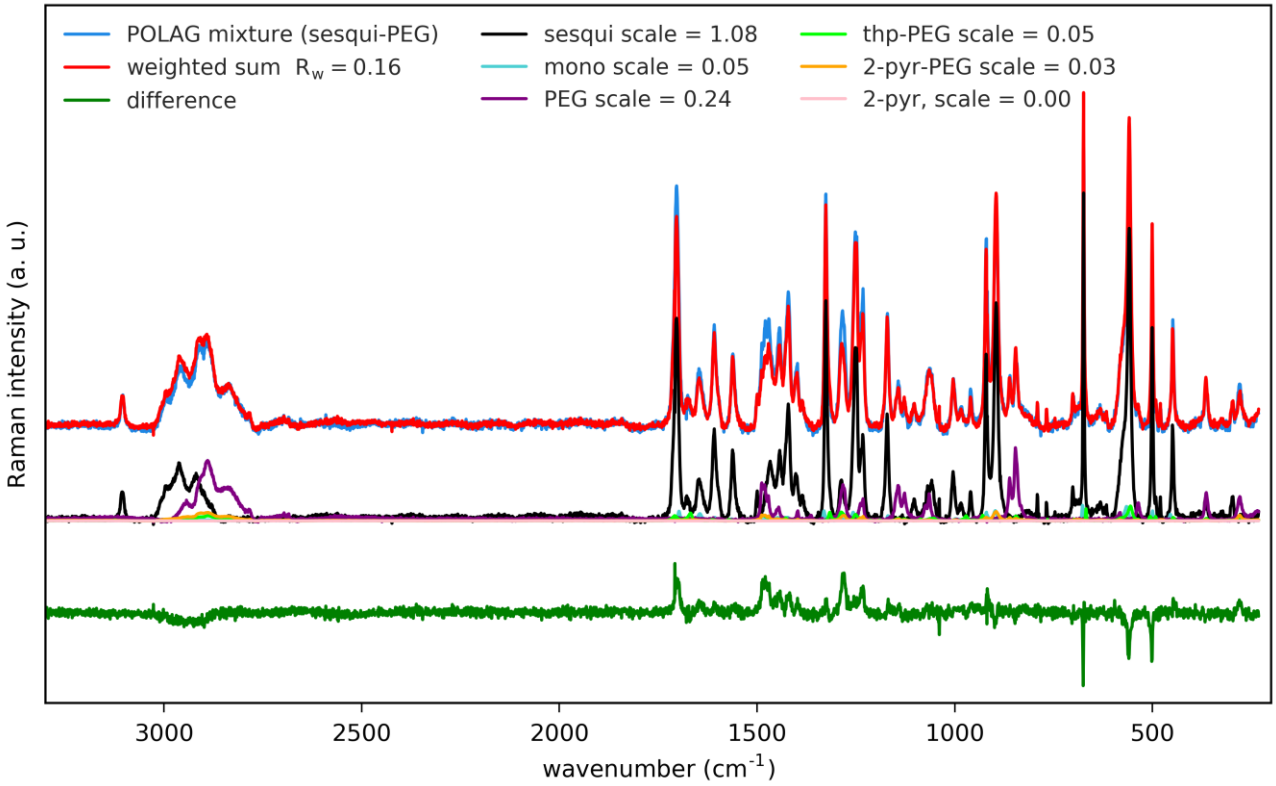

Figure S52: Pattern indexing of the Raman spectrum of the POLAG mixture of **sesqui** -PEG using the spectra of the pure components and binary mixtures. The indexing suggests that the predominant contributions are from **sesqui** and the polymer.

5. Computational Study

5.1. Computational Methods

All calculations in this section were performed with Materials Studio using the COMPASS-II forcefield with its own atomic charges.

Molecular model generation. Molecular models for **thp** and **2-pyr** were retrieved from their CSD crystal structures (NILYAI and BAPLOT respectively). For the polymers, small polymers containing either 3 or 4 monomers were generated manually using the Materials Studio visualizer. For PEG, three monomers were linked together to make a PEG_3 model as shown in Figure S52. For PAA and PAAm, four monomers were used in all cases to generate PAA_4 and $PAAm_4$ oligomer models. With regards to the tacticity of the PAA_4 and $PAAm_4$ models, the same tacticity was used in both models consisting of a u-d-u-u sequence where u and d refer to the different orientation of the functional group within the polymer chain.

Generation of conformers for the polymers. Next, the most stable conformers for all polymer models (PEG_3, PAA_4 and $PAAm_4$) were explored using the Conformer Generator model. For this, a random sampling algorithm was used and up to 3000 conformers were generated per polymer model always using geometry optimization as part of the generation process. The most stable conformer for all polymers was then taken forward.

Geometry optimization of molecular models. All molecular models were then geometry optimised in the gas-phase using the COMPASSII forcefield. For the polymers, the energetics of the most stable conformers were taken forward (E_{mol}).

Geometry optimization of crystal models. All relevant crystal structures were retrieved from the CSD including the crystal structures of the **thp**:**2-pyr** sesquisolvate (PICMIA), the **thp**:**2-pyr** monosolvate (PICMOG) and the crystal structure of the most stable **thp** polymorph (BAPLOT01, form II). All crystal structures were geometry optimised allowing for the atomic positions as well as the unit cell parameters to change. The lattice energy per crystal system was then calculated by

$$E_{latt} = \left(\frac{E_{cell}}{N_{cell}^{main}} - \sum_i n^i E_{mol}^i \right)$$

where N_{cell}^{main} is the number of molecules of the main component in the unit cell, *i* refers to each of the components in the unit cell, E^i_{mol} is the gas-phase molecular energy for each of the components and *n* is the stoichiometry of component *i* relative to one mol of the main component. The lattice energy thus is calculated per mol of the main component in kJ/mol.

Amorphous models. The Amorphous Cell module was used to construct amorphous models for the three pure polymers and the co-amorphous systems for the three polymers together with **2-pyr**. For each of the systems, the amorphous model was generated in the following way.

a. The generation of the amorphous system was done using a cubic cell with a low target density of 0.5 g/cm^3 and a load of 30 oligomers for the pure polymer system and 30 oligomers with 30 **2-pyr** molecules for the co-amorphous system. This resulted in generated initial models of between 25×25×25 to 35×35×35 Å^3 dimensions depending on the system. The construction algorithm, which uses a Monte Carlo based model, was then run at 300 K optimizing the structures after generation whilst keeping the unit cell parameters constrained to maintain the target density. 100 different models were generated per system with the model with the lowest energy taken for further simulations.

b. The lowest energy amorphous model with low density 0.5 g/cm^3 was then subjected to molecular dynamics simulations at constant volume. The system was equilibrated for 500 ps at 300 K in the NVT

ensemble using the Nose Thermostat with a time step of 1 fs. In this step, the oligomer-oligomer and oligomer-**2-pyr** interactions were allowed to equilibrate and optimise in this low-density system.

c. After the NVT equilibration at 300 K, the system was then subjected to NPT simulations also at 300 K. The system was then equilibrated for another 500 ps at 300K in the NPT ensemble using the Nose Thermostat and the Berendsen Barostat with a time step of 1 fs. In this step, the density increased considerably from the 0.5 g/cm^3 to up to ~1.1 g/cm^3.

d. The last structural cell of the NVT-NPT simulations was then taken for geometry optimization. The energy of the amorphous model was then calculated in the same fashion as the lattice energy, by

$$E_{amorph} = \left(\frac{E_{cell}}{N_{cell}^{main}} - \sum_i n^i E_{mol}^i\right).$$

For the co-amorphous models, a 1:1 stoichiometry was used in a simulation cell with 30 molecules of oligomer and 30 molecules of **2-pyr**.

5.2. Computational Results

Whilst the crystal structures of the **thp**:**2-pyr** sesquisolvate, monosolvate and the theophylline crystals are well known, the structure of the polymers are not readily available since these are amorphous with the exception of PEG which can also be crystalline.

For modelling the polymers a number of assumptions/approximations were made. First, the polymers were simplified by using a shorter chain model for all of them – thus effectively simulating oligomers rather than polymers. For PEG three monomers were used to generate a PEG_3 model whilst for PAA and PAAm four monomers were used to generate PAA_4 and $PAAm_4$ molecular models. A number of conformations were generated for these (see methods) and the most stable conformation of each of those PEG_3, PAA_4 and $PAAm_4$ models was used as reference for their molecular energy.

Next, amorphous models were produced for these three oligomers as well as 1:1 oligomer:**2-pyr** co-amorphous models as explained in the methods. And optimised. Optimisation of the amorphous models together with the known crystal structures of theophylline, the MONO and the SESQ allowed for the calculation of lattice (E_{latt}) as well as amorphous (E_{amorp}) energies for all systems.

Next, the energy of the reactions taking place by mechanochemistry were then estimated making use of the Lattice and Amorphous energies of the reactions and products. Thus, to calculate the energy of the reactions, the lattice/amorphous energies of the reactants were subtracted from the lattice/amorphous energies of the products using the correct stoichiometries by

$$E^{reaction} = \sum_{products} n^i E_{latt/amorph}^i - \sum_{reactants} n^i E_{latt/amorph}^i .$$

where n^i are the stoichiometric proportions of the systems involved. In our case, stoichiometries have been adjusted so that the reaction energy is calculated per mol of **2-pyr** transferred between phases. The mechanochemical reaction, reactants, products and calculated reaction energies for all systems are summarised in table 3. Here, when the reaction energy is negative it means that the products are more stable than the reactants and thus the reaction should take place. This is of course an approximation since we are only able to compute energies of reaction and not free energies. Since all components remain in the solid state (either as a crystal or amorphous) and similarly reactants and products consist of a crystal as well as an amorphous solid, it is reasonable to assume that the entropies of reactants and products would be similar.

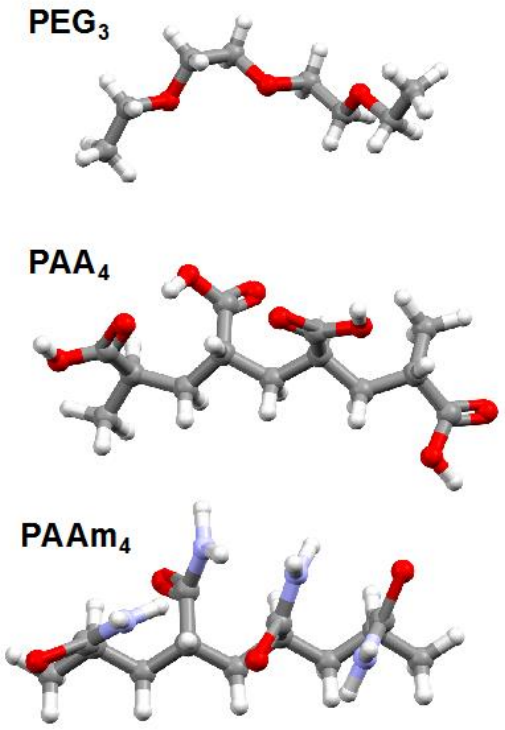

Figure S53: Molecular structures of the polymers used for the simulations.

Table S2: The mechanochemical reaction, reactants, products and estimated reaction energies for all systems in this work.

Reaction	Reactants	Products	Reaction Energy (kJ/mol)*
Sesq converts to Mono in the presence of PEG	2 $(SESQ)_{crys}$ + $(PEG)_{amorph}$	2 $(MONO)_{cryst}$ + $(PEG.Pyr)_{amorph}$	-1
Sesq converts to Mono in the presence of PAAm	2 $(SESQ)_{crys}$ + $(PAAm)_{amorph}$	2 $(MONO)_{cryst}$ + $(PAAm.Pyr)_{amorph}$	-6
Sesq converts to Mono in the presence of PAA	2 $(SESQ)_{crys}$ + $(PAA)_{amorph}$	2 $(MONO)_{cryst}$ + $(PAA.Pyr)_{amorph}$	-27
Mono converts to Theo in the presence of PEG	$(MONO)_{crys}$ + $(PEG)_{amorph}$	$(THEO)_{cryst}$ + $(PEG.Pyr)_{amorph}$	8
Mono converts to Theo in the presence of PAAm	$(MONO)_{crys}$ + $(PAAm)_{amorph}$	$(THEO)_{cryst}$ + $(PAAm.Pyr)_{amorph}$	3
Mono converts to Theo in the presence of PAA	$(MONO)_{crys}$ + $(PAA)_{amorph}$	$(THEO)_{cryst}$ + $(PAA.Pyr)_{amorph}$	-18

*Normalised per mol of **2-pyr**.

6. References

1. A. A. Coelho, *Journal of Applied Crystallography*, 2018, **51**, 210-218.
2. P. J. Chupas, X. Qiu, J. C. Hanson, P. L. Lee, C. P. Grey and S. J. L. Billinge, *Journal of Applied Crystallography*, 2003, **36**, 1342-1347.
3. A. P. Hammersley, S. O. Svensson, M. Hanfland, A. N. Fitch and D. Hausermann, *High Pressure Research*, 1996, **14**, 235-248.
4. P. Juhás, T. Davis, C. L. Farrow and S. J. L. Billinge, *Journal of Applied Crystallography*, 2013, **46**, 560-566.
5. X. Yang, P. Juhás, C. L. Farrow and S. J. L. Billinge, *arXiv*, 2015, **arXiv:1402.3163v3**.
6. A. A. Coelho, P. A. Chater and A. Kern, *Journal of Applied Crystallography*, 2015, **48**, 869-875.
7. D. Hasa, M. Pastore, M. Arhangelskis, B. Gabriele, A. J. Cruz-Cabeza, G. S. Rauber, A. D. Bond and W. Jones, *CrystEngComm*, 2019, **21**, 2097-2104.